

University of Duisburg-Essen · Campus Duisburg

Faculty of Engineering

Department of Mechanical and Process Engineering

Institute for Product Engineering · Division of Manufacturing Technology

Bachelor Thesis

for attainment of the academic degree of

Bachelor of Science in Mechanical Engineering

Influence of Process Parameters on Element Distribution and Magnetic Properties of $\text{Ni}_{78.5}\text{-Fe}_{21.5}$ prepared by Laser Beam Melting

Hanna Schönrath

Matriculation Number: 3009289

from Duisburg

November 2, 2017

submitted to Prof. Dr.-Ing. Gerd Witt
Prof. Dr. rer. nat. Michael Farle

supervised by Dr.-Ing. Jan T. Sehart
Dr. Marina Spasova

Abstract

In this work the influence of the process parameters in Laser Beam Melting (LBM) on the element distribution and magnetic properties of Permalloy ($Ni_{78.5} - Fe_{21.5}$) was studied. Therefore, iron and nickel powders were mixed and used to build 25 samples with different process parameter sets and volume energy densities. Three characteristic samples were chosen and further investigated. The surface analysis with scanning electron microscope (SEM) and energy dispersive X-ray spectroscopy (EDX) indicated line-shaped surface segregations of iron and nickel at a high volume energy density of $E_v = 428.57 \frac{J}{mm^3}$. For the bulk material, this lead to a homogeneous element distribution. The formation of a $FeNi_3$ phase was indicated by an XRD measurement. At lower volume energy density and in the powder a Ni phase was found. The analysis with EDX and vibrating sample magnetometer (VSM) showed a more homogeneous element distribution and an increase of the saturation magnetization M_s up to 14% in the case of the sample processed with high energy related to the initial powder blend.

In dieser Arbeit wurde der Einfluss der Prozessparameter des Laser Strahlschmelzprozesses auf die Elementverteilung und die magnetischen Eigenschaften von Permalloy ($Ni_{78.5} - Fe_{21.5}$) untersucht. Dazu wurden 25 würfelförmige Testkörper mit unterschiedlichen Prozessparametern aus gemischtem Eisen- und Nickelpulver hergestellt. Aus diesen wurden drei beispielhafte Körper ausgewählt und näher untersucht. Die Oberflächenanalyse mit dem Raster-Elektronenmikroskop (REM) einschließlich EDX zeigte eine linienförmige Segregation der beiden Elemente bei einer Volumenenergiedichte von $E_v = 428.57 \frac{J}{mm^3}$. Für den innenliegenden Bereich führte diese Energie stattdessen zu einer $FeNi_3$ -Phase, welche mit einer XRD Messung gezeigt wurde. Die Analyse via EDX und VSM zeigte, dass bei steigender Volumenenergiedichte im Bauprozess die Elementverteilung homogener und die Sättigungsmagnetisierung um bis zu 14% gesteigert wird, ausgehend vom gemischten Pulver zur Probe mit dem höchsten Energieeintrag.

Aufgabenstellung

Bearbeiter: Hanna Schönrath

Betreuender Universitätsprofessor: Prof. Dr.-Ing. habil. G. Witt

Betreuender Mitarbeiter: Dr.-Ing. Jan T. Sehr

Thema:

Influence of Process Parameters on Element Distribution and Magnetic Properties of Ni_{78.5}-Fe_{21.5} prepared by Laser Beam Melting

Aufgabenstellung:

In der Vergangenheit wurden bereits unterschiedliche Werkstoffe für das Laser-Strahlschmelzen (LBM, Laser Beam Melting) unter den Gesichtspunkten der mechanischen Belastbarkeit, Maßhaltigkeit und Güte qualifiziert. Jedoch ist das Wissen über den Einfluss verschiedener Prozessparameter auf die magnetischen Eigenschaften in ferromagnetischen Werkstoffen derzeit begrenzt. Ziel dieser Arbeit ist daher die Untersuchung des Einflusses der Volumenergiedichte auf die Homogenität der Elementverteilung und auf die magnetischen Eigenschaften. Als Ausgangswerkstoff sollen die beiden nahezu reinen Pulver, bestehend aus Ni bzw. Fe, exemplarisch charakterisiert und im Verhältnis 78,5 at.-% Ni zu 21,5 at.-% Fe ($Ni_{78.5} - Fe_{21.5}$) gemischt und anschließend im Laser-Strahlschmelzprozess mit unterschiedlichen Volumenergiedichten verarbeitet und analysiert werden. Anhand von ausgewählten Parametersätzen sollen Bauteile zur genauen Bestimmung von strukturellen und magnetischen Eigenschaften hergestellt werden. Die Ergebnisse sollen anschließend mit den LBM-Parametern korreliert werden.

Versicherung an Eides Statt

Ich versichere an Eides statt durch meine untenstehende Unterschrift,

- dass ich die vorliegende Arbeit - mit Ausnahme der Anleitung durch die Betreuer - selbstständig ohne fremde Hilfe angefertigt habe und
- dass ich alle Stellen, die wörtlich oder annähernd wörtlich aus fremden Quellen entnommen sind, entsprechend als Zitate gekennzeichnet habe und
- dass ich ausschließlich die angegebenen Quellen (Literatur, Internetseiten, sonstige Hilfsmittel) verwendet habe und
- dass ich alle entsprechenden Angaben nach bestem Wissen und Gewissen vorgenommen habe, dass sie der Wahrheit entsprechen und dass ich nichts verschwiegen habe.

Mir ist bekannt, dass eine falsche Versicherung an Eides Statt nach § 156 und nach § 163 Abs. 1 des Strafgesetzbuches mit Freiheitsstrafe oder Geldstrafe bestraft wird.

(Ort, Datum)

(Student)

Contents

1	Introduction	1
2	Theoretical Background	3
2.1	The Process in Theory	3
2.1.1	Introduction to Additive Manufacturing	3
2.1.2	Laser Beam Melting	3
2.2	Introduction to Magnetism	6
2.2.1	Types of Magnetism	7
2.3	The Material Permalloy	10
2.3.1	General Properties	10
2.3.2	Magnetic Properties	11
3	Experimental Procedure	13
3.1	Preparation and Characterization of the Raw Material	13
3.2	Preparation of Samples by LBM	14
3.2.1	Machine Setup	14
3.2.2	Choice of Process Parameters	14
3.2.3	Design of the Samples	15
3.3	Surface Characterization	15
3.4	Characterization of Bulk Material	16
3.5	X-ray Diffraction	17
3.6	Magnetometry	18
4	Results and Discussion	20
4.1	Characterization of the Powder	20
4.2	Production of Samples	22
4.3	Surface Analysis	23
4.3.1	High Energy Input	27
4.3.2	Adequate Energy Input	28
4.3.3	Low Energy Input	28
4.4	Analysis of Bulk Material	29
4.5	Density and Pores	31
4.6	Crystal Phase Analysis	32
4.7	Analysis of Magnetic Properties	34
5	Conclusions	39

List of References	41
List of Figures	44
List of Tables	46
Appendix	47

1 Introduction

The fabrication of magnetic materials using the branch of additive manufacturing methods, informally 3D-printing, is subject to this thesis and other recent investigation due to the advantages given by new possibilities in design, free choice of orientation and reusable raw materials.

Additive manufacturing (AM) processes commonly assemble products by the layer-wise addition of material. This technology is mainly used for rapid prototyping, applying the advantage of fast and individual production. Recently, there have been researches aiming at introducing new materials and improving precision while lowering production costs. Thereby the quality of the process improved and the possibility for rapid manufacturing, i.e. the production of final parts in low batch sizes, with AM has been emerging. The results find their applications especially in engineering, e.g. for the production of prototypes, lightweight parts or complicated mesh-shaped structures, and in medicine, e.g. for individualized implants. But apart from these already established sectors, different fields of application are still under investigation. Especially concerning the use of specific materials, great effort is put into the determination of suitable process parameters for granting a high quality of the resulting products. The materials that can be currently processed include the range of polymers, ceramics, sand, paper and metal. [1, 2, 3, 4]

Focusing on metallic materials, the commonly available alloys cover only a small range of titanium, nickel, aluminium and chrome alloys, as well as stainless steel. These materials can be purchased in the shape of powder with spherical grains of a machine-specific size to ensure a reliable process. Not all materials used in conventional manufacturing can be supplied in the needed shape and few powders were tested and characterized for AM. This characterization involves the specification of the raw material and of suitable process parameters for the reliable production of high-quality parts. Recently the interest has been expanding to magnetic materials, which have specifics in application, e.g. in electric motors, but also in production due to interference with machine parts. Apart from hard magnetic materials that are used for permanent magnets and often include expensive rare earth elements [5], soft magnetic materials are also of interest. For instance, they find their application in sensors. With the advantage of near net-shape production, the number of post-processing steps can be reduced along with the amount of material wasted by cutting processes. AM enables the possibility to tailor these materials, not only according to their shape and design, but also their material properties. B. Zhang [6] showed that the choice of process parameters, namely the variation of the scanning speed, influences the magnetic properties. Furthermore, T. Bauer et al. [7] showed the effects of the process parameters on the element distribution in the binary NiFe system using mixed powders. The effect of these changes in homogeneity on magnetic properties was

not evaluated. Therefore, this thesis should combine the two aspects with the aim of relating the energy input during the production to the resulting element distribution and magnetic properties of additively manufactured permalloy, an alloy of 78.5 at.-% Ni and 21.5 at.-% Fe. Therefore, the raw material of mixed iron and nickel powder is used to produce samples with different process parameters, which are then investigated according to their structural and magnetic properties.

2 Theoretical Background

2.1 The Process in Theory

For the production of the samples the laser beam melting process is used. It is categorized as a powder bed fusion method and belongs to the Additive Manufacturing processes.

2.1.1 Introduction to Additive Manufacturing

Manufacturing processes which add material successively (layer-wise) to build up the shape of a body are generally called "Additive Manufacturing" (AM), commonly also referred to as "3D-Printing" [4]. An advantage of AM is the possibility to create individualized near net shaped structures and complex geometries directly from a CAD model, which are impossible to realize with other processes [3, 4]. The orientation of the object during the building process can be chosen freely, therefore the anisotropy direction can be varied or support structures can be applied at the best possible positions. Furthermore, there are no specific product-related tools needed to generate the objects. That means without changing the setup of the machine, different shapes can be produced simultaneously. Open hollow shapes, undercuts, casting moulds and tools with integrated cooling channels can be manufactured while simultaneously decreasing material consumption [8, 9]. Besides the positive aspects, AM has mainly two disadvantages: Firstly the surface roughness of R_z between $90\text{ }\mu\text{m}$ and $150\text{ }\mu\text{m}$ [1] is relatively high compared to e.g. $R_z \approx 2.5\text{ }\mu\text{m}$ achieved by precise milling [10]. Secondly, support structures are needed to hold overlapping geometries and ensure a good heat transfer especially in metal melting processes. The need of these support structures reduces the freedom of design and the surface quality of the final part.

Nowadays, Additive Manufacturing is used for the production of prototypes (rapid prototyping), of ready-to-use products and even tools (rapid manufacturing / tooling) directly from a 3D CAD model [9]. Application fields are found in areas such as medicine for individualized implants and surgery preparations, aerospace engineering for lightweight constructions, in metallurgy for creating forms for casts and in design engineering for creating prototypes [3, 11].

2.1.2 Laser Beam Melting

The process used in this work for the sample fabrication is called "laser powder bed fusion of metal powders" or short "Laser Beam Melting (LBM)", which are multisupplier designations [12]. It is a process optimized for the manufacturing of metallic powders, reaching high temperatures to melt the powder grains and inducing high cooling rates of up to $10^6\text{ }^\circ\text{C/s}$. The building

process takes place in a powder bed by melting the metallic particles with a laser. Depending on the literature and company, different names are used. Examples are "Selective Laser Melting" (SLM Solutions), "Direct Metal Laser Sintering" (Fa. EOS GmbH) and "Laser Cusing" (Concept Laser). [1, 13]

Procedure

The complete operation during the production of a final part or prototype can be separated into pre-processing, the main process and post-processing. The usually performed steps are schematically depicted in figure 2.1.

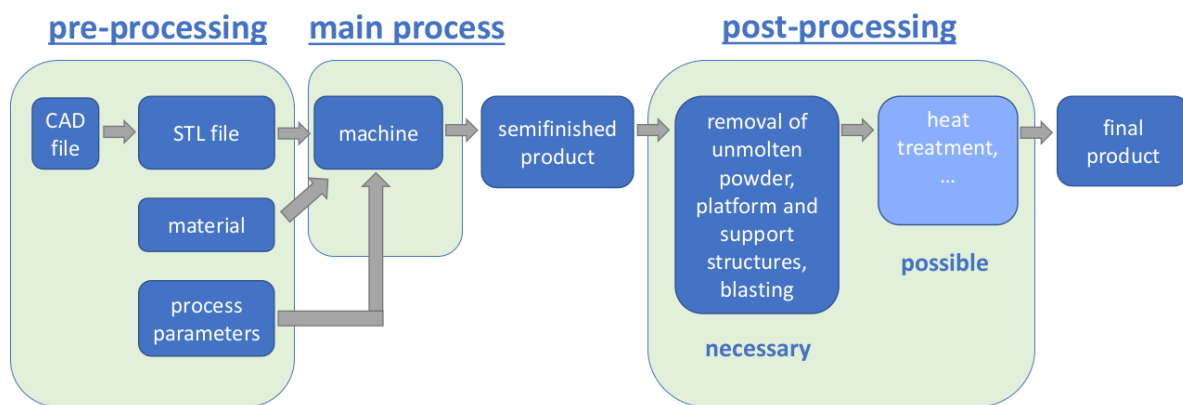


Figure 2.1: Sketch of the process steps for laser beam melting

Pre-processing includes all necessary steps to enhance the conceptualized idea into a processable product. Firstly, a CAD-model has to be created which then is converted into an STL file. This format displays the surface geometry with triangles and is compatible with most of the regular machines. The STL file is converted into a machine-specific format by slicing which means that the designed part is saved as a combination of its horizontal cross-sections. These are representing the single layers of the part. Parameters concerning the accuracy of the model, e.g. the size of the triangles used for triangulation and the layer thickness for slicing as well as the parameters for the building process should be chosen properly. These are named scanning velocity, laser power, beam diameter, hatch distance and layer thickness and they will be further explained in chapter 2.1.2.

The main process is similar for most AM machines based on powdered materials. The build platform is set exactly on the starting level. A container supplies the powder, which is distributed evenly on top of the platform by a coating blade. In the next step, the laser beam selectively melts the first layer of the powder in the areas defined as the cross-section of the part in the sliced data format. Afterwards, the platform is lowered to avoid a collision of the molten layer and the blade when it returns to the initial position. These steps are repeated until the sample

is finished. [1, 14]

Finally, in the post-processing the loose material of the powder bed is removed manually with a brush. This powder can be sieved and then reused for other building processes. The platform is withdrawn from the machine and cleaned with compressed air. The desired parts are separated from the platform and (if necessary) from the support structures. By blasting, unmolten powder attachments on the surface are removed. Furthermore, post-processing steps can be added for instance to reach a higher ductility or hardness by heat treatment. [1, 3]

The process is influenced by numerous variables, which can partly be controlled. For example, the air humidity during the process or the storage atmosphere of the powder are usually not measured. The most important variables for this work are the adjustable process parameters of the method as well as the material. Influences of the surroundings and post-processing steps will not be considered.

Process Parameters

The process principle is schematically shown in figure 2.2. The following adjustable process parameters are depicted: The scanning velocity v_s , laser power P_L and diameter d_s of the laser beam as well as the scanning strategy. Concerning the powder supply, the amount of available powder per coating and the thickness of the applied powder layer D_s can be varied.

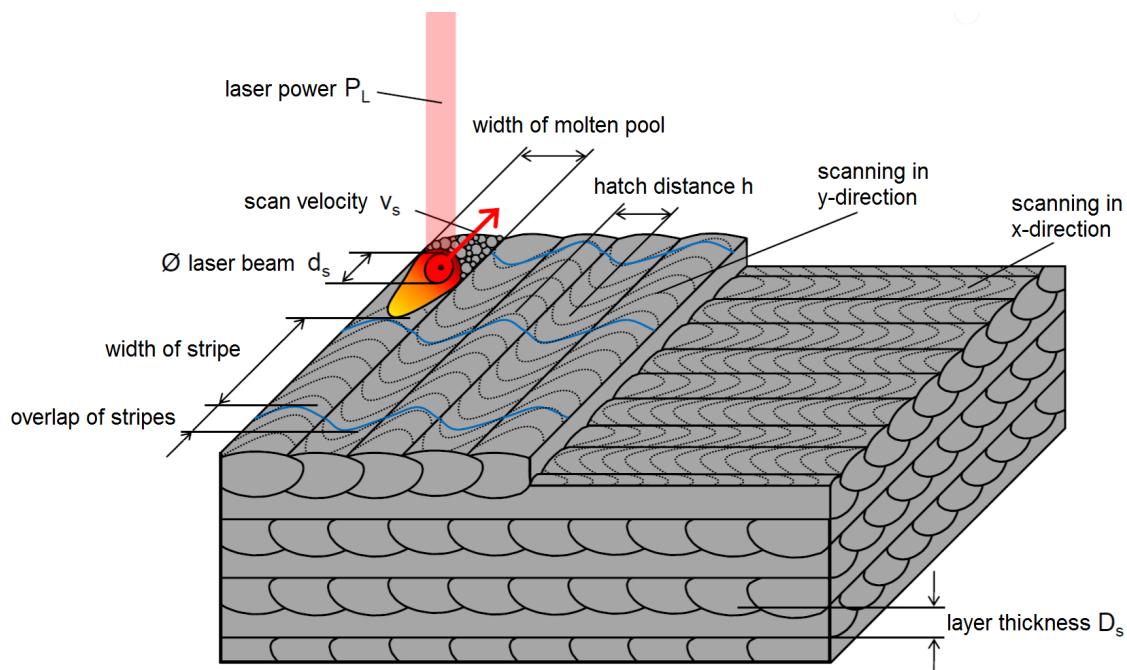


Figure 2.2: Process parameters in Laser Beam Melting for a bi-directional alternating stripe scanning strategy. In a single layer, the laser scans the surface stripe-wise in positive and negative scan axis. This axis is alternating between x and y axis for each new layer [1]

The scanning strategy describes the path of the laser beam. It can be mono- or bidirectional,

as depicted in figure 2.2. The overlap of stripes is the area which was molten twice to ensure the connection of the separately scanned stripes. The scan axis can be fixed for all layers or alternating at certain angles. Often, the alternating scanning strategy is used, which means that in every new layer the direction of the scan rotates by 90° . The alternating rotating scanning strategy also can be used, where the direction is rotated by 67° referring to the last layer to prevent repeating the same direction of scan in every second layer. Thus possible anisotropies within the x-y-plane can be eliminated. The laser can scan the surface by running over the full width of the part, in single stripes or in squares. There may be different scanning parameters for the contour and the inside to achieve a better surface quality, called contouring.

As a general reference for the energy input into the layer of powder, the volume energy density E_V is introduced by Meiners [15]:

$$E_V = \frac{P_L}{v_s \cdot h \cdot D_s} \quad (2.1)$$

where P_L is the laser power, v_s the scanning velocity, h is the hatch distance and D_s the layer thickness. The value of E_V should enable a comparison of process parameters between different AM machines, so that the relation of the process parameters to the resulting product properties can be transferred to other systems. The machines usually differ in their possible adjustment ranges of laser power, scanning velocity and laser beam diameter, hence the process parameters need to be adapted according to the capabilities of the machine.

As commonly known in production, the quality of the product in LBM is mainly determined by the choice of raw material. Besides the composition, its morphology is mainly influencing the process. The shape, grain sizes, density and flowability are the most important factors in LBM. In general, to grant flowability and thereby achieving optimal results, the grains should be spherical and of a small particle size range. [1, 2, 13]

2.2 Introduction to Magnetism

In order to evaluate the magnetic properties of additively manufactured permalloy, the basic concepts of magnetism will be explained here.

Magnetism is a physical phenomenon, which leads to the interaction of bodies with magnetic fields [16]. The resulting magnetic forces are well-known due to their applications in every-day life, reaching from simple fridge-magnets to computer memories and sensors. One commonly observed effect is the Lorentz-Force: Charged particles moving through a magnetic field experience a force orthogonal to the direction of motion and to the field. Vice versa, moving charges also create a magnetic field [17].

A measure for the strength of a magnetic source is the magnetic dipole moment m and its volume average $M = \frac{m}{V}$, which is called volume magnetization. The magnetic field is described by the field strength H and a material's response to the applied external field is described by the flux density B . In a vacuum they are related by the permeability of free space μ_0 . In general, the following relation holds [18]:

$$B = \mu_0(H + M) = \mu_0\mu_r H = \mu H \quad (2.2)$$

where μ_r is the relative and μ the general magnetic permeability. The susceptibility χ for materials with linear response of the volume magnetization M to the external field H is introduced as:

$$\chi = \frac{M}{H} = \mu_r - 1 \quad (2.3)$$

The magnetic permeability and susceptibility are related as they both display the material-specific ease of magnetization. A high permeability physically means that the material responds in low external fields H with a high flux density B . The total magnetic moment of an object specifies the intensity of its reaction to an external field. As the object consists of atoms, its moment is the sum of the atomic moments, which themselves are the sum of the contributions of its electrons. The orbital angular momentum, which establishes because of the electrons' circular movement around the nucleus, and the spin angular momentum, which is a purely quantum mechanical phenomenon and can be described as internal momentum of an electron, contribute to the atomic moment. The Pauli principle and the Hund rules describe how electrons occupy the orbitals. If a shell is completely filled, each orbital holds two electrons. They differ only in their spin, which can point either up- or downwards, so that in an atom with completely occupied shells and therefore two electrons in each orbital the resulting effective angular moment is zero. In atoms with an odd number of electrons the total angular moment is not zero and hence the atom possesses a magnetic moment. [17, 18]

2.2.1 Types of Magnetism

Due to different reactions of materials to an applied magnetic field, the following types of response can be differentiated:

Ferromagnetism

In ferromagnetic materials, the magnetic moments of the atoms are unequal zero and tend to orientate in the same direction as the neighboring moments, so that the state of lowest energy level within the system is obtained. This quantum-mechanic coupling effect is called exchange interaction, and it is a strong, but short-range effect. As a result, regions with parallel

aligned magnetic moments form, which are called domains. They differ in the direction of their moment in such a way that the total magnetic moment of a ferromagnetic body is zero in the initial, demagnetized state, to minimize the total energy of the ferromagnet. The walls of the domains are movable, although their displacement needs to be driven by an energy input. If this energy is applied in the form of an external field H , the domain walls move and thereby the domains with an orientation along H grow while others shrink. Finally, with a strong external field, all magnetic moments are aligned and the saturation magnetization M_s is reached. The values of μ and χ are not constant, but functions of H . The more the field is reduced afterwards, the more the domain's orientations tend to flip back to energetically more suitable directions. Nevertheless, the motion of domain walls consumes energy and the initial state of zero magnetization cannot be reached by removing the external field. The remanence M_r is the magnetization of the sample when the external field is reduced to $H = 0$ after reaching the saturation magnetization. Therefore, a counteracting external field needs to be applied. The strength of this opposing field that leads to a complete demagnetization ($M = 0$) of the material is called coercivity or coercive field H_c . If the counteracting field is increased further, the domains will orientate in the opposite direction and finally the saturation magnetization is reached again, now negatively oriented. Thereby, ferromagnetic materials exhibit a hysteretic magnetization curve. The general ferromagnetic hysteresis loop is displayed in figure 2.3. [17, 18, 19]

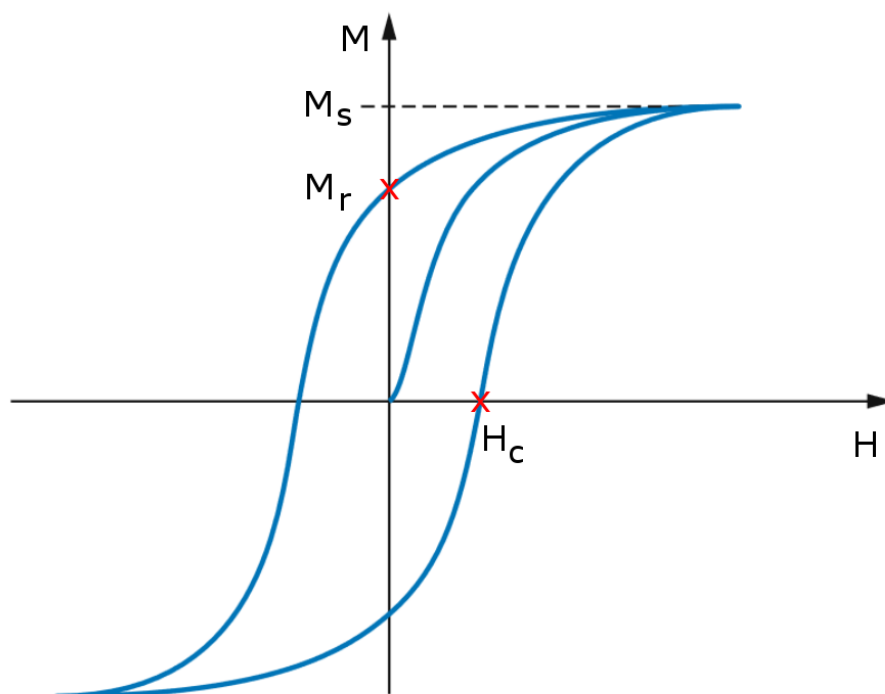


Figure 2.3: Hysteresis of a ferromagnetic material showing the magnetization M in dependence on the external field H with saturation magnetization M_s , remanence M_r and coercive field H_c [20]

For ferromagnetic materials, the magnetic anisotropy should be considered. On a microscopic

scale, the magnetocrystalline anisotropy influences the orientation of magnetic moments of atoms. In the crystal structures easy and hard axis exist and the moments tend to orientate along the easy axis. To reach an alignment along the hard axis, a higher energy input is required. The domains often do not exceed the grain boundaries, which represent a change in lattice orientation.

The macroscopic shape of the body influences the magnetization of a body. This is called magnetic shape anisotropy, and this phenomenon is also related to the internal energy minimization. The magnetization of a body consumes less energy, if the resulting stray field outside of the material is reduced. The greater the field becomes, the greater is also the effort needed to establish the magnetization. For example, a long beam can easily be magnetized lengthwise, but not widthwise. As a further influencing factor, the change of a ferromagnetic body's dimensions in an external magnetic field, which is named magnetostriction, should be mentioned. This effect causes strains in the material. Stresses, as the result of magnetostriction or also of mechanical machining and loading, cause an anisotropic behavior of the material. For a material with a negative magnetostriction coefficient in the case of pressure the easy axis is parallel to the line of pressure, whereas in the case of tension the easy axis is perpendicular to the force. Nickel for example has a negative magnetostriction coefficient. When samples for the magnetometric analysis are removed from the building platform it should be considered that the mechanical work can cause a change in the anisotropy behavior. [18, 17]

The group of ferromagnetic materials can be subdivided into hard and soft magnets. They are distinguished by their magnetic anisotropy energy. Hard magnets with a high crystalline anisotropy have a high remanence and a coercivity of $H_c > 10000 \frac{A}{m}$. They are usually used as permanent magnets due to the fact that they cannot be demagnetized easily. A good example is the material neodymium iron boron ($Nd_2Fe_{14}B$). In comparison, soft magnets have a low coercivity and low magnetocrystalline anisotropy, but a high permeability and susceptibility. The reason is the low energy needed to move domain walls. The magnetization can be changed easily. Therefore, soft magnets are commonly used for electromagnetic cores, motors and also for magnetic shielding. [17]

With rising temperature, the movement of atoms increases, which is lowering the effectiveness of the exchange interaction between the atoms. Therefore, at higher temperatures the saturation magnetization decreases, until it reaches zero at the Curie-Temperature T_C . Above this temperature, the material behaves paramagnetic. [17]

Iron, nickel and cobalt, so called 3-d transition elements, are ferromagnetic a room temperature.

Paramagnetism

In comparison to ferromagnetism, the exchange interaction in paramagnetic materials is not strong enough to overcome the thermal energy, hence the atomic magnetic moments do not align. Although each atom has a non-zero magnetic moment, they cancel each other out due to the thermal fluctuation so that the total magnetic moment reduces to zero without an external field. Therefore, the magnetization increases linearly with an increasing external field of low intensity, as each single atom's moment orientates along the external field. The susceptibility is generally weak in comparison to the ferromagnetic one, and if no external field is applied, the total magnetization of a paramagnetic body is zero. [17]

Examples for paramagnetic materials are aluminum and titanium.

Diamagnetism

If the atomic moment of an element is zero, the material response to an external field is diamagnetic. This means that it sets up a weak opposing field. This means the relative permeability μ_r is smaller than one and χ is negative. The charges tend to shield the inside of the body from the magnetic field.

Most organic materials behave weakly diamagnetic and so do noble gases with their fully occupied shells. Superconductors are ideal diamagnets with the highest possible diamagnetic susceptibility of $\chi = -1$. It means the complete absence of magnetic permeability and the exclusion of the interior magnetic field. [17, 18]

2.3 The Material Permalloy

The nickel-based alloys in the range of Fe - 70-85 at.-% Ni are called permalloys, due to the strikingly high initial permeability they can achieve at high cooling rates [21]. In this work the focus is set on Permalloy with 21.5 at.-% Fe and 78.5 at.-% Ni.

2.3.1 General Properties

Permalloy has a face-centered cubic (fcc) structure at room temperature. The density is approximately $8.4 \frac{\text{g}}{\text{cm}^3}$. The mechanical properties show no unexpected behavior and little reactions to heat treatment, in contrast to the magnetic properties, which depend strongly on the cooling rate [22]. According to the phase diagram of the binary iron nickel system, which is shown in figure 2.4, in equilibrium at room temperature the $FeNi_3$ phase is stable at the composition of Permalloy, (78.5 at.-% Ni). In this region the $L1_2$ superstructure can establish, which means that a chemically ordered atomic structure forms above the face centered cubic

(fcc) structure. In this superstructure, the Ni atoms are placed on the faces and Fe atoms on the corners. In the disordered state, every position can be occupied by a Fe atom with a probability of 75% or by a Ni atom with a 25% probability.

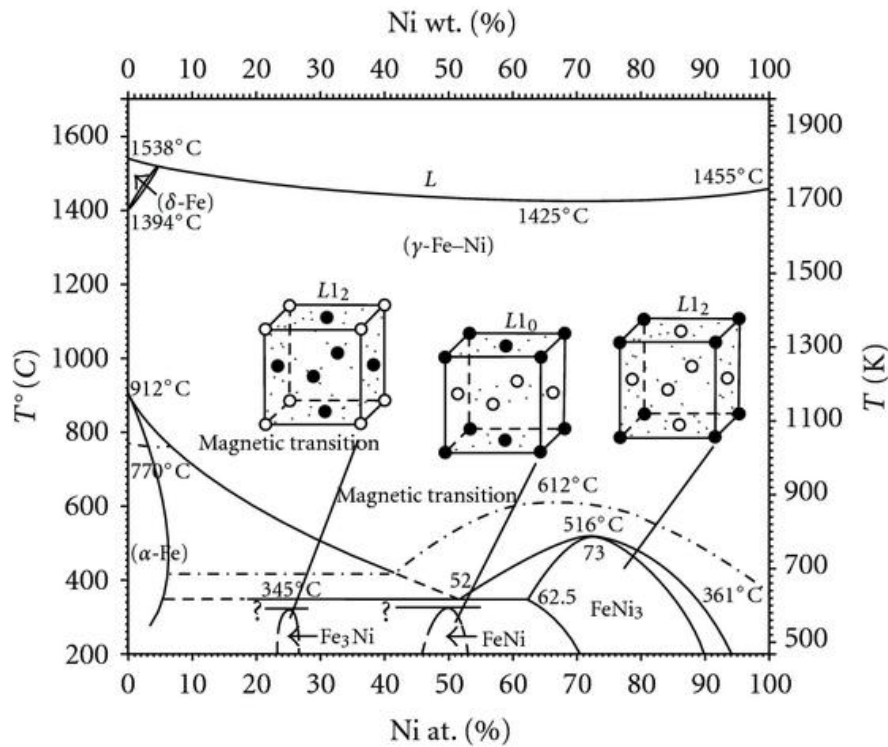


Figure 2.4: The binary phase diagram of the Fe-Ni system with superstructures (\circ = Ni, \bullet = Fe) [23]. At 78.5 at.-% Ni a $FeNi_3$ phase and the L_{12} superstructure can be expected

2.3.2 Magnetic Properties

Permalloy is a soft ferromagnetic material. The magnetocrystalline anisotropy and magnetostriction are small. It has a high initial permeability of $10^4 \mu_0$ and the coercivity is around $8 \frac{A}{m}$. These properties are strongly dependent on the type of heat treatment, as can be seen in figure 2.5 for the initial permeability, stated by a study of Elmen et al. [22]. In this study three different heat treatments were applied to ring-shaped samples:

- cooling from over $900^\circ C$ with a cooling rate of $\approx 1.5^\circ C/min$, which is called annealing,
- annealing plus reheating the sample to $600^\circ C$ and rapidly cooling it with a rate of $\approx 20^\circ C/sec$, called air quenching,
- annealing plus reheating to $425^\circ C$ and holding the sample at this temperature for 24 h, called baking.

At low cooling rates a superstructure can establish, which causes differences in material properties. By quenching the chemical order can be reduced, which is accompanied by a high

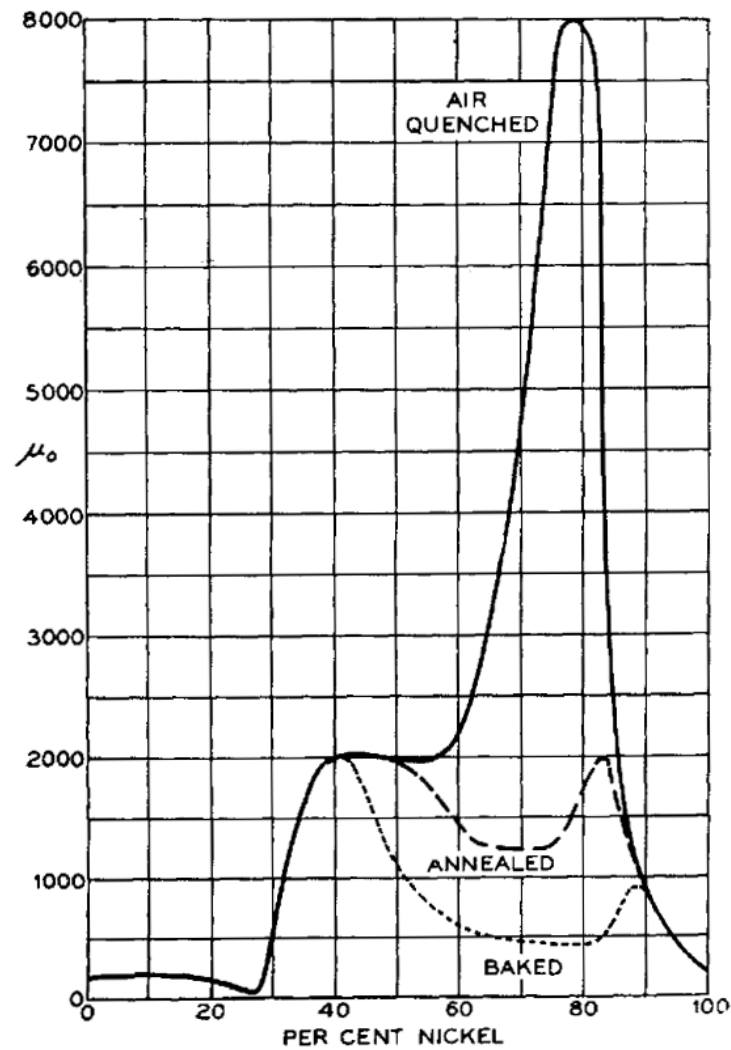


Figure 2.5: Effect of heat treatment and composition on initial permeability of nickel-iron-alloys for air quenched (cooling rate of $20^\circ\text{C}/\text{sec}$), annealed ($1.5^\circ\text{C}/\text{min}$) and baked (held at 425°C for 24h) alloys [22]

permeability. In industrial use alloying elements like copper, chrome or molybdenum are added to achieve the same effect. [18, 22, 23, 24]

For bulk permalloy a saturation mass magnetization of $\approx 110\text{Am}^2/\text{kg}$ and a coercivity of 8 kA/m can be expected at room temperature. By quenching from 600 to 25°C the coercivity is expected to be reduced. [25]

3 Experimental Procedure

In this chapter the general proceedings of the experiments as well as principles and specific properties of the measurement devices are explained. The experiments include the characterization and mixing of the initial metal powders, the building process of the samples, and a surface analysis as the basis for a grouping of samples with similar properties. Representatives of these groups are used for further examination of horizontal and vertical cuts considering structure, phase, density, element distribution and magnetic properties. By applying the aforementioned methods to the two cuts of the cubes the properties of the bulk material are approximated. Additionally the magnetic properties of samples with the representative process parameters are measured.

3.1 Preparation and Characterization of the Raw Material

The shape, size distribution and purity of a nickel and an iron powder are investigated. Thereafter, the mixing process is performed by a hand-driven powder mixer according to the Turbula principle with a glass container for 30 minutes. Powder mixers according to the Turbula principle use a combination of translational, rotational and inverse motion to achieve a homogeneous mixture of powders [26]. To ensure a good mixing behavior, samples are taken every 5 min and investigated with SEM and EDX. The thereby found mixing ratio r of atomic % iron to nickel is compared to the desired one, which is given as:

$$r_d = \frac{at \% Fe}{at \% Ni} = \frac{21.5 \%}{78.5 \%} = 0.274 \quad (3.1)$$

Three measurements at different positions on each sample are taken to calculate the mean ratio. Additionally the powder is checked for the formation of agglomerations with a light microscope.

The apparent density of the well mixed powder is then determined with the funnel method [27]. Therefore, a funnel is filled with powder, which is flowing into a standardized cup. The weight of the powder inside the cup is measured as m and the volume of the cup is $V = 25 \text{ mm}^3$. The apparent density is the calculated mean value of three measurements and is given as

$$\rho_{ac} = \frac{m}{V} = \frac{m}{25 \text{ mm}^3} \quad (3.2)$$

Subsequently, the flow rate of the powder is measured according to the Hall flowmeter measurement [28]. Therefore, 50 g of powder is placed in a standardized funnel and the time between the moment of opening the funnel and the moment of the last powder grains leaving it is measured.

3.2 Preparation of Samples by LBM

3.2.1 Machine Setup

For this work the machine EOS M 100 was used. It is a smaller version of an industrial powder bed fusion laser beam melting machine. The building chamber, the optical unit, the process gas supply, the powder container and the blade are mounted on a slideable structure. In the process, a specific amount of powder is dropped in front of the blade. Then the whole construction slides sideways while the blade distributes the powder on the circular building platform. The remaining powder is captured in a container behind the platform. When the blade reaches the other side, the superstructure including the optical unit and the process gas supply and discharge cover the platform completely. Nitrogen is supplied to the building chamber to prevent the oxidation of metals at high temperatures and the laser beam locally melts the powder. Afterwards, the platform is lowered and the construction slides back to the initial position. The procedure is repeated, until the part is finished and can be removed from the machine. The powder containers and building chamber are removable to enable a fast change of different materials without the need of time-consuming cleaning of all parts of the machine. The settings of the EOS M 100 are as follows: The steel building platform is circular with a diameter of 100 mm. The build-in laser is a Yb fibre laser with a laser beam diameter of $d_s = 30 \mu m$. [14]

3.2.2 Choice of Process Parameters

According to previous work by Zhang et al. [6], Shishkovsky et al. [29] and Bauer et al [7], a broad set of parameters for the first building process is chosen, resulting in a testing range for E_V between 30 and 430 $\frac{J}{mm^3}$, given in table 3.1. The laser power and scanning velocity are varied, while the hatch distance is chosen as $h = 70 \mu m$ and the layer thickness as $D_s = 20 \mu m$. The alternating rotating scan strategy without contouring is used, and the building platform is not preheated. The surfaces of these first samples are investigated with SEM and EDX to find suitable parameter sets for further experiments.

Table 3.1: Selected process parameters for the LBM building process

$E_V \left(\frac{J}{mm^3} \right)$		$v_s \left(\frac{mm}{s} \right)$				
		100	200	300	400	500
$P_L (W)$	20	142.86	71.43	47.62	35.71	28.57
	30	214.29	107.14	71.43	53.57	42.86
	40	285.71	142.86	95.24	71.43	57.14
	50	357.14	178.57	119.05	89.29	71.43
	60	428.57	214.29	142.86	107.14	85.71

3.2.3 Design of the Samples

The design of the samples is adapted to the needs of the analysis methods. Two sizes are chosen and displayed in figure 3.1: Cuboids with 7.5 mm edge length and 5 mm height are taken for the characterization of the structure and the element distribution, whereas cubes of 3 mm edge length suffice for the magnetic measurements. The reduced size is needed due to restrictions of the measurement device, whereas the cubic shape is chosen to reduce the effect of magnetic shape anisotropy at different orientations of the magnetic measurements (see p. 18). To enable a mechanical removing of the 7.5 mm cuboids from the building platform without applying a high force and thereby possibly inducing magnetostriction with changes in anisotropy, support structures are applied. At the bottom additionally 2.5 mm of material is produced as four dense blocks, which are converging downwards. They are built with the same process parameters as the samples themselves. The support structure for the 3 mm cubes is substituted by an additional 1 mm of dense material. After the mechanical removal of the building platform, the cubes are cut to the desired 3 mm length.

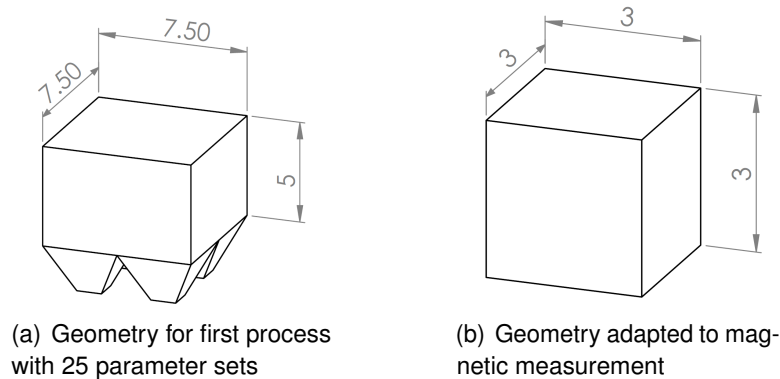


Figure 3.1: CAD design of the samples, dimensions are given in mm

The post-processing includes the removal of loose powder and the mechanical separation of the cubes from the building platform. No further treatment of the surface is performed.

3.3 Surface Characterization

To investigate the microstructure and especially the shape of welding lines of the samples, a scanning electron microscope (SEM) is used. Energy dispersive X-ray spectroscopy (EDX) is included in the LEO 1530 SEM and is used to determine the local and global elemental composition of the samples surfaces.

In an SEM, an electron beam is used to image the surface of a sample. Therefore, a field emission gun is used as an electron source. The emitted electrons are accelerated by an applied electric field and the resulting electron beam is focused on a sample's surface with

magnetic and electrostatic lenses. When the beam hits the sample, different types of radiation are caused, for instance X-rays, backscattering and secondary electrons. The backscattering electrons can be registered by an in-lens detector. If the electron beam scans the surface of the sample, the energy of the backscattered electrons of each scanned point is registered. This data is used to display an electron image of the sample's surface. Thus imaging at the scale of micro- and nanometers is possible. Contrast in the images may occur due to local changes in topography, material, crystal orientation, internal or external magnetic field of the sample. Material contrast for instance means that depending on the atomic number of the material, the corresponding image is of a lighter shade for heavier materials and vice versa. Nevertheless, the topology of the surface has the highest influence on the contrast. Alternatively, a secondary electron detector can be used for receiving a higher topology contrast. [30]

An EDX spectrometer can be used to detect the energy of X-rays resulting from the interaction of the electron beam of the SEM with the sample surface. When the electron beam impacts the surface, some of the electrons perform inelastic scattering interactions with the sample atom's electrons. These are thus ejected from the atomic shell, leaving a space which is filled by another electron from a higher orbital. The difference between the energy levels of the electron's position on the outer shell and its new position on an inner shell is released in form of an X-ray with a specific wavelength and energy portion. The EDX detects the energy of the X-rays and presents the measured spectrum. Information from a database can be added and thus the registered peaks in the spectrum can be related to elements occurring at the measured surface. EDX can be used for measuring the general material composition of an area or a spot, or for registering the local occurrence of elements in a mapping. In this work the mapping function is mostly used to show the occurrence of single elements with different colors. [30]

The measurement depth of SEM and EDX can be simulated by the program "Casino" which uses the Monte Carlo approach [31]. The performed measurements have a simulated maximum depth of 800 nm. Thus they are surface sensitive measurement methods, the results that are measured at the upper surface cannot be claimed to depict the properties of the bulk material. Depending on the surface structure and element distribution measured on the uncut samples by SEM and EDX, a reduced number of representative samples is chosen for further experiments.

3.4 Characterization of Bulk Material

The analysis of the approximate structure in the bulk material is performed by applying surface sensitive measurements (SEM and EDX, light microscopic density, XRD) at the horizontal and vertical cuts of the samples with 7.5 mm edge length, as shown in figure 3.2. The cuts are performed by a diamond equipped blade with water cooling. Afterwards, the cut samples are embedded in the compound Technoterm 3000. They are smoothened by grinding and polishing

up to a roughness of $1\ \mu\text{m}$.

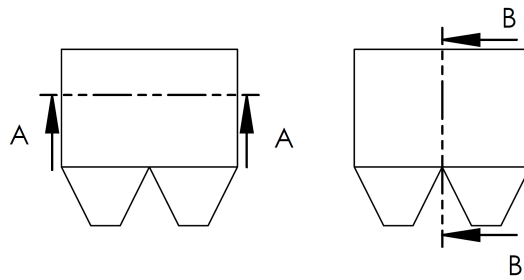


Figure 3.2: Sketch of the directions of cut: Horizontal A-A and vertical B-B

The approximate density is determined with the image analysis of metallographic specimens according to VDI guideline 3405 [12]. This porosity analysis method uses light microscopic pictures to perform a binary image analysis. The percentage of pixels displaying the material expresses the density of the sample. This is used to compare the density of the chosen representative samples and of the different cuts A-A and B-B of each sample. The software Stream Essentials by Olympus is used, where this method is also called "phase analysis ". Furthermore, the distribution of iron and nickel on the horizontal and vertical cuts is investigated with EDX measurements.

3.5 X-ray Diffraction

X-ray diffraction (XRD) is used to analyze the crystal structure and phase of the samples. The device includes an X-ray tube and an aperture which produce a focused X-ray beam of the wavelength $\lambda = 1.54056\ \text{\AA}$. It reaches the sample surface at the angle θ . At the atoms on this surface the X-rays are reflected. In a polycrystalline material the atoms are ordered in atomic planes of a distance close to the wavelength λ of the X-rays and the reflection happens not only on the uppermost plane but on several planes in the material. Due to the resulting angle-dependent optical path difference for reflected radiation at the first and a higher order planes, interference can be observed. The condition for this diffraction is given by Bragg's Rule. It correlates the angle of the n -th interference maximum to the sample's lattice constant d with a given wavelength of the X-rays λ : $2d \sin \theta = n \cdot \lambda$. By detecting the intensity of the reflected radiation a diffractogram is generated. The obtained data can be compared to a database in order to determine the phase of the sample.[19]

Here the Bragg-Brentano geometry is used, which is schematically depicted in figure 3.3 [32]. In this setup the sample is placed in the center of a focal circle. The X-ray tube and the detector move around the sample in the same angle θ on the focal circle. The apertures are adjusted to enable the detection of the complete sample surface at all angles θ . The measurement is performed on the polished vertical cuts A-A (see figure 3.2).

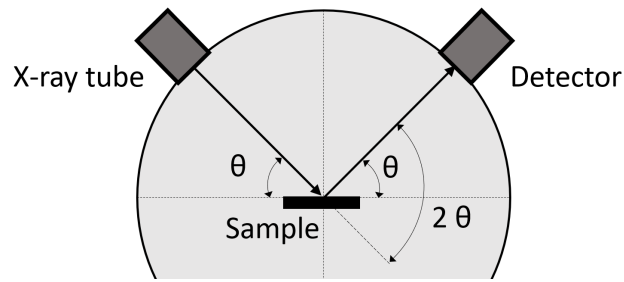


Figure 3.3: Bragg-Brentano geometry for XRD. The X-ray tube and the detector move around the sample with the angle θ

3.6 Magnetometry

For the magnetic characterization of the samples, the Vibrating Sample Magnetometer (VSM) is used. The setup is schematically given in figure 3.4.

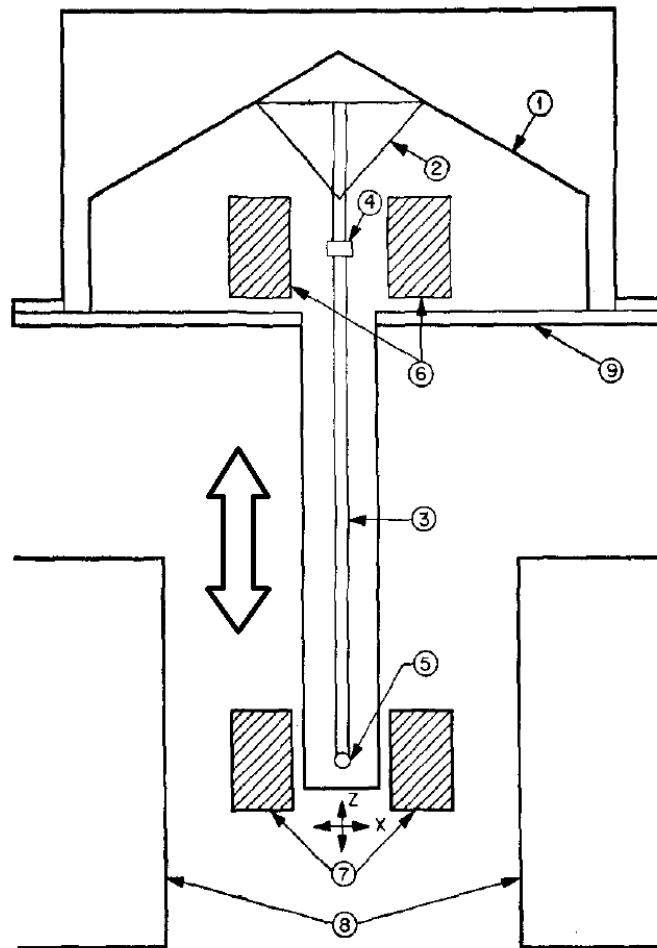


Figure 3.4: Sketch of a Vibrating Sample Magnetometer including a reference sample. (1) transducer, (2) inlet support, (3) sample holder, (4) reference sample, (5) sample, (6) reference coils, (7) sample coils, (8) field-inducing magnet poles, (9) metal container [33]

The VSM consists of a long straw-shaped sample holder, which can be vibrated vertically. The sample is placed between two field-inducing coils or magnets. They cause a homogeneous

external field with an intensity that can be varied. The sample will respond with a change in magnetization. Within two smaller pick-up coils, the vibrating sample causes an induced voltage, which relates to its magnetization. The changes in magnetization are detected and the results can be used to display the sample's magnetization in dependence to the external field. This output is divided by the mass of the corresponding sample. Hence, it is given as the mass magnetization, not as the volume magnetization.

Due to the size of the device and mainly the distance between the coils, the sample size is restricted to a maximum of about 3 mm, depending on the orientation and shape. [33]

The measurements are performed in dependence to the orientation during the LBM building process. For the parallel measurements the external field is applied along the z-axis, for the perpendicular measurements it is orthogonal to the z-axis (see figure 3.5). The measurements are performed at 300 K, corresponding to room temperature.

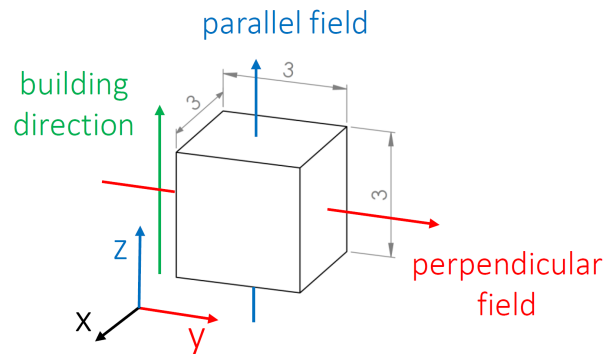


Figure 3.5: Orientation of sample cube in VSM: The parallel external field is oriented along the building direction z, the perpendicular field orthogonal to it

4 Results and Discussion

4.1 Characterization of the Powder

Firstly, the two single powders of iron and nickel were characterized. According to the manufacturer, the iron powder has a purity of 99.8% and a d_{50} of $29.53\ \mu\text{m}$, the nickel powder has a purity of 99.7% and a d_{50} of $30.10\ \mu\text{m}$, both are of a spherical shape. To evaluate this data, the powder is analysed with SEM and EDX.

The size and shape of the powder particles was analyzed by evaluating ten SEM pictures of each powder. The diameter of all visible particles was measured, resulting in the size distributions given in figure 4.1. These distributions are similar for iron and nickel and show their maxima at a diameter between 5 and $15\ \mu\text{m}$ in the relative number distribution and between 30 and $45\ \mu\text{m}$ in the relative volume distribution. In figure 4.2 (a) it can be seen that the shape of the nickel powder grains is mostly spherical. Some particles have smaller satellite particles attached to their surfaces. The iron powder shown in (b) is mostly spherically shaped as well, but seems to have a higher number of small particles, which tend to agglomerate.

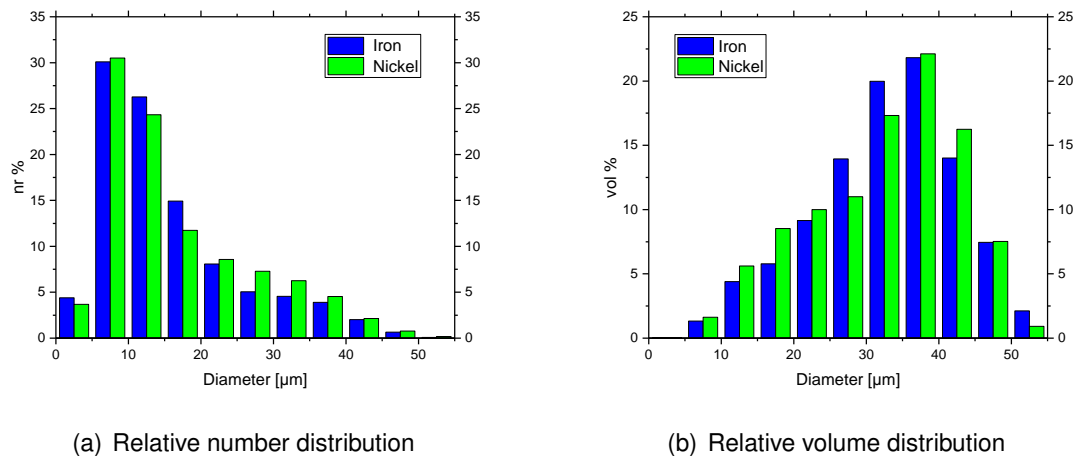


Figure 4.1: Size distributions of the single input powders, based on analysis of 10 SEM pictures for each element

Samples taken after the mixing process were investigated with a light microscope to detect possible agglomerations. It could be seen that the agglomerations that seem to exist are rather caused by multiple layering of particles. They are not stable and collapse when touched. In figure 4.3 (a) a corresponding picture is given. The iron and nickel particles differ in color, iron appears silver, while nickel is colored bronze.

With the EDX mapping a precise distinction of the particles is possible, as can be seen in figure

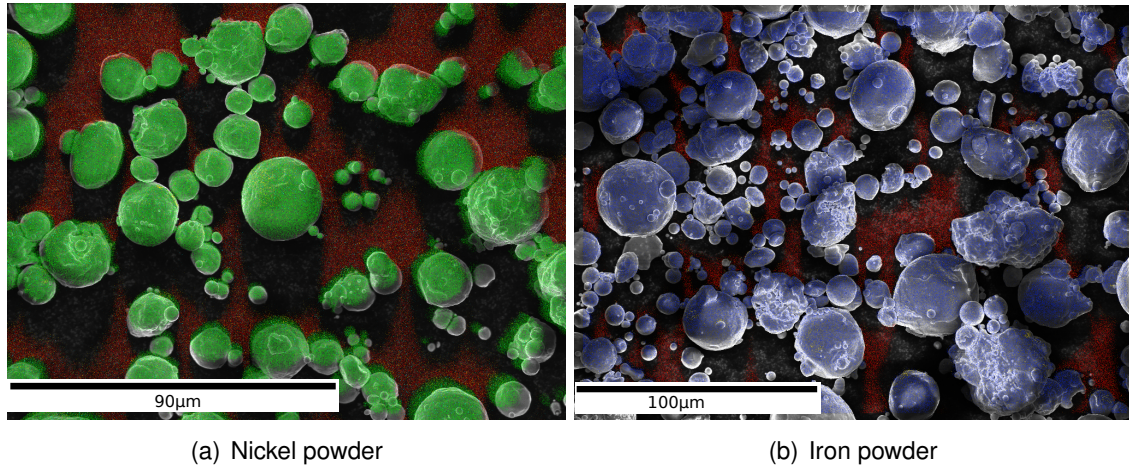


Figure 4.2: Size and shape of input powders particles. Colors: Fe = blue, Ni = green, C = red

4.3 (b). Here, five frames were taken and the registered pixels were multiplied by 4 before coloring, to receive coherently colored and distinguishable particles. The two types of particles are mixed and the iron particles are distributed mostly evenly across the nickel particles.

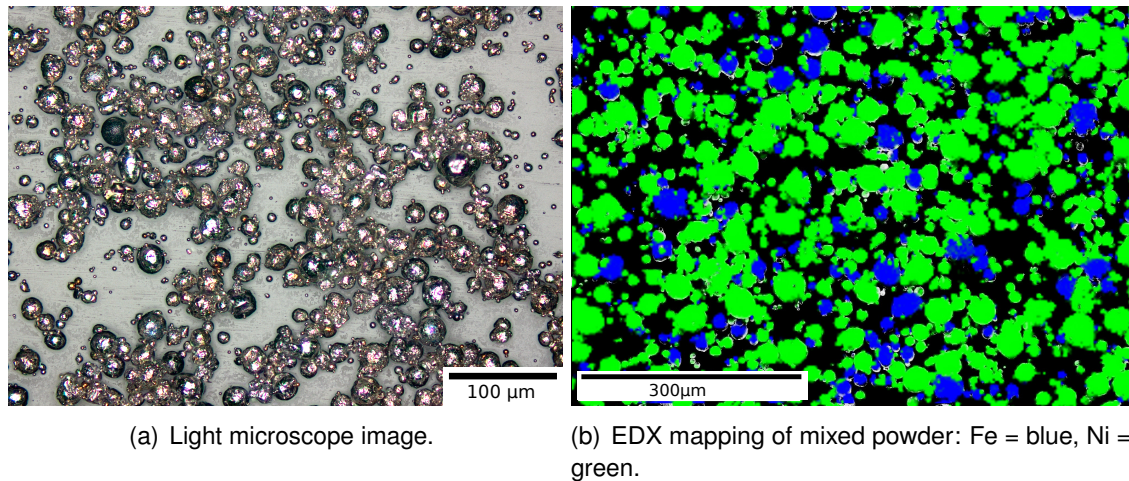


Figure 4.3: Particle distribution in the mixed powder after 30 min mixing

To document the quality of the blend, the mixing ratio according to equation (3.1) was measured with EDX depending on the mixing time. The results are shown in figure 4.4. After 25 min the desired mix was established and although the standard deviation is in the same order as the measured values, a well mixed powder supply for the additive manufacturing process is hereby assumed.

The apparent density according to equation (3.1) was measured as $\rho_{ap} = \frac{208 \text{ g}}{25 \text{ cm}^3}$. The mean time an amount of 50 g powder needs to flow through the funnel was measured as 4.5 s, thus the approximated flow rate is $\frac{5 \text{ s}}{50 \text{ g}}$.

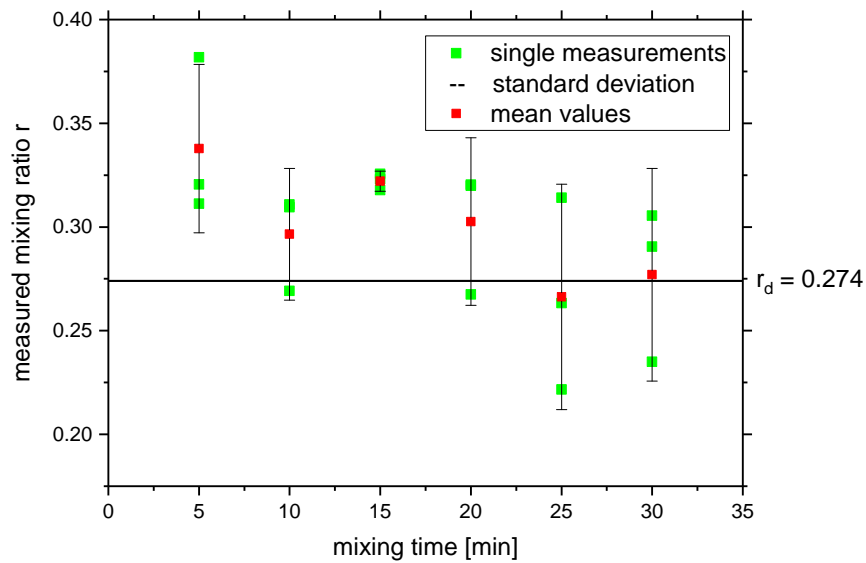


Figure 4.4: Variation of the measured mixing ratio r depending on the mixing time. After 25 min the mixture approaches the desired ratio of 0.274 according to equation (3.1)

4.2 Production of Samples

The metallic blade and powder feed roll supplied by the manufacturer show magnetic interactions with the mixed powder. Thus, a ceramic blade and a polymer feed roll which had to be manufactured by laser sintering were inserted in the EOS M 100 machine for the building process.

The build platform with the produced samples is shown in figure 4.5. The values for E_v are given in table 3.1. The two samples with the lowest value for the energy input (top right corner in figure 4.5) had to be deleted as their single layers were not connected firmly. The samples were removed mechanically without causing high deformations. An exception are the samples with the lowest energy input, where the support structures broke due to a weak connection of the processed layers.

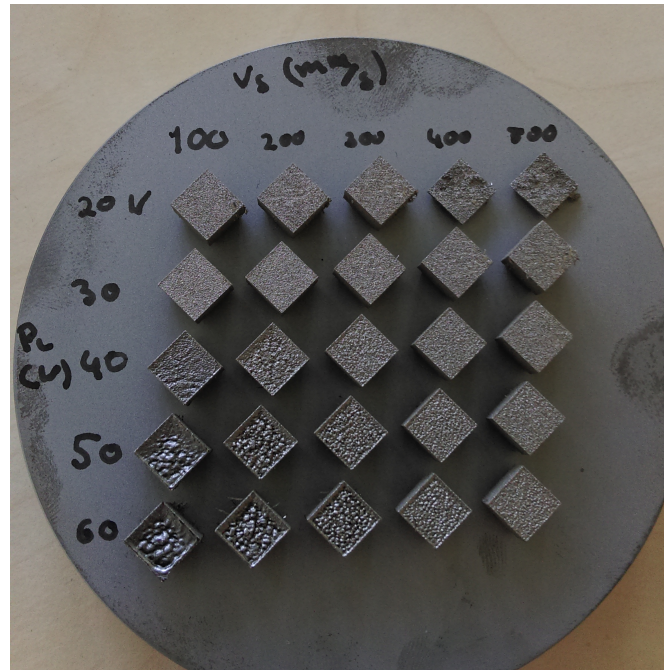


Figure 4.5: Photo of the platform with built samples before separating the samples from the platform. Parameters: $P_L = 20 \text{ W}$ to 60 W and $v_s = 100 \text{ mm/s}$ to 500 mm/s . Different surface structures are visible, especially at high energy input a surface swelling can be seen

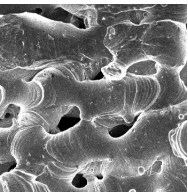
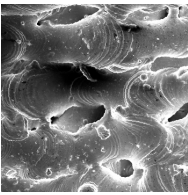
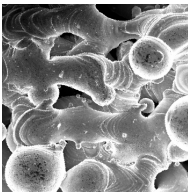
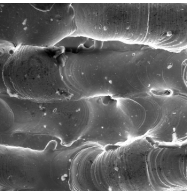
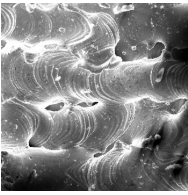
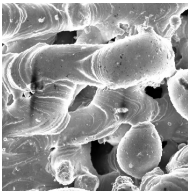
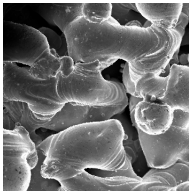
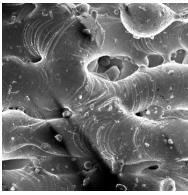
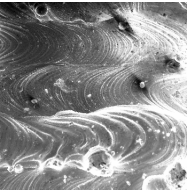
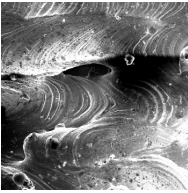
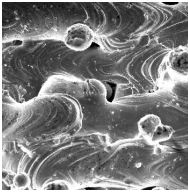
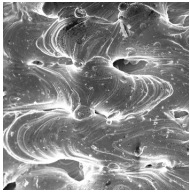
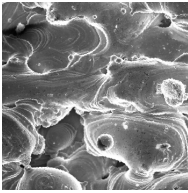
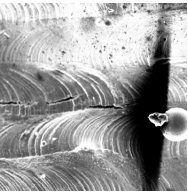
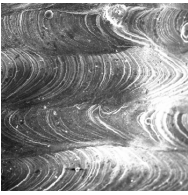
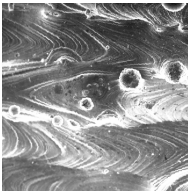
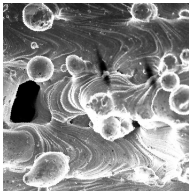
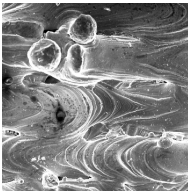
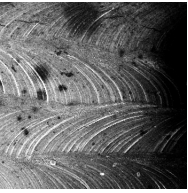
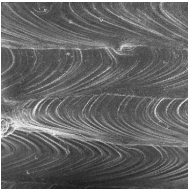
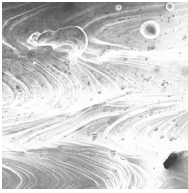
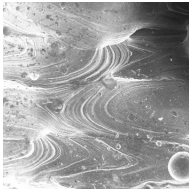
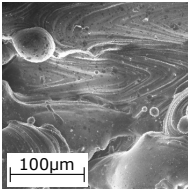
4.3 Surface Analysis

The surfaces of the produced samples are analyzed to find three suitable parameter sets with low, medium and high volume energy density for a detailed investigation of the structure, element distribution and magnetic properties. Analysis criteria are the quality of the welding lines, the general surface structure and the distribution of elements. For the optimal parameter set, the welding lines should be slightly overlapping and of an even structure, no pores or weld beads should occur. The element distribution should be homogeneous and without segregations.

The welding lines for the produced samples are depicted in table 4.1. Focusing on the low energy inputs first, at $P_L = 20 \text{ W}$ the welding lines are irregularly shaped and hardly recognizable. Almost no overlap can be seen and a structure of high porosity was formed. When the volume energy density E_v is increased, the thickness of the welding lines increases. Thus, they are well connected and form a dense structure. At a further increase to 60 W laser power the welding lines strongly overlap, which is an indicator for an energy input that is greater than necessary.

It is striking that samples produced with the same E_v but with a different combination of laser energy and scanning speed do not show the same surface structures. Thus, the laser power and scanning velocity have different influences on the microstructure. However, this will not be considered further in this thesis.

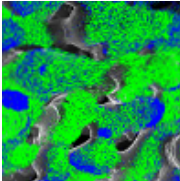
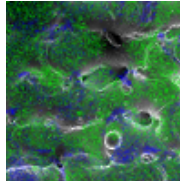
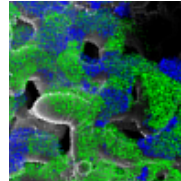
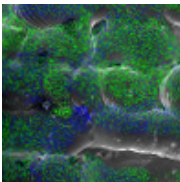
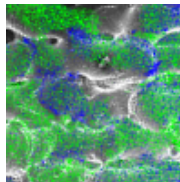
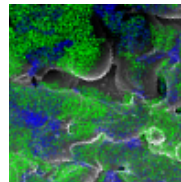
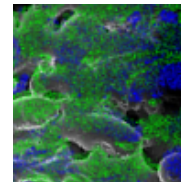
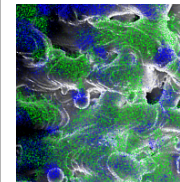
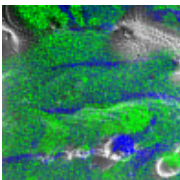
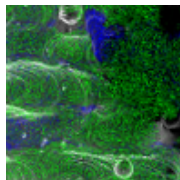
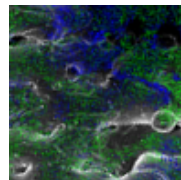
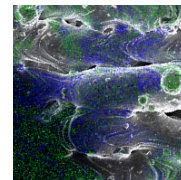
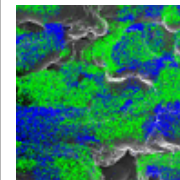
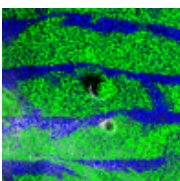
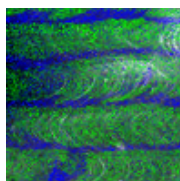
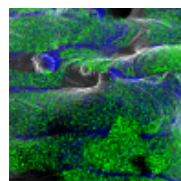
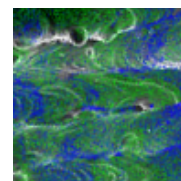
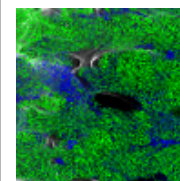
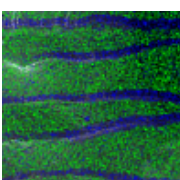
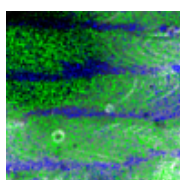
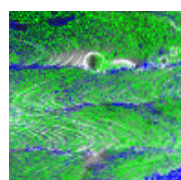
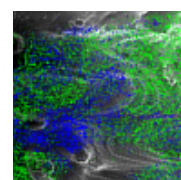
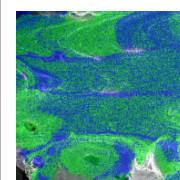
Table 4.1: SEM-pictures in dependence on the used laser power and scanning velocity during the building process

$P_L v_s$	100 mm/s	200 mm/s	300 mm/s	400 mm/s	500 mm/s
20 W				not built	not built
30 W					
40 W					
50 W					
60 W					

The distribution of the elements on top of the samples varies with the energy input, which can be seen in table 4.2. At lower input, especially at 20 W laser power, the elements are not mixed. Instead, areas with high amounts of nickel are clearly separated from areas with high amount of iron. With increasing E_v the distribution of the elements becomes more homogeneous, which can be seen at 60 W and 500 mm/s or at 50 W and 500 mm/s. The highest energy input, however, leads to a line-shaped segregation of iron and nickel. This can be seen at the bottom left corner of table 4.2. Within the welding lines mainly nickel can be found, while at the edges the iron concentration is increased with respect to the desired ratio. This segregation is investigated further with a second mapping of higher resolution, which is shown in figure 4.7 and will be discussed later.

Combining the morphology and element distribution on the sample's surfaces, four groups of parameter sets are classified. Figure 4.3 schematically depicts the groups of samples showing

Table 4.2: EDX mappings of samples produced with different laser powers and scanning velocities showing the occurrence of nickel (green) and iron (blue)

$P_L v_s$	100 mm/s	200 mm/s	300 mm/s	400 mm/s	500 mm/s
20 W				not built	not built
30 W					
40 W					
50 W					
60 W					

a similar surface structure and element homogeneity. The uncolored samples could not be built due to a very low energy input. Samples colored in blue have a low energy input resulting in a porous structure and non-mixed elements; Sample C with $E_v = 47.62 \frac{J}{mm^3}$ is chosen as a representative for this group. The green samples are produced with an adequate energy input leading to a rather dense structure and more homogeneous distribution of elements. For this group, sample B with $E_v = 71.34 \frac{J}{mm^3}$ is chosen as representative. At last the samples with a high E_v are colored in red, showing the characteristic line-shaped segregations of the elements. Sample A with $E_v = 482.57 \frac{J}{mm^3}$ depicts these characteristics well and is selected for further testing.

In table 4.3 the three representative samples A, B and C are shown. For each sample, a detailed SEM picture and the corresponding EDX mapping is shown next to a macroscopic picture of the upper surface. The differences can be clearly seen due to the high porosity of sample C, the line-shaped segregation of A and the rather even macroscopic structure of B.

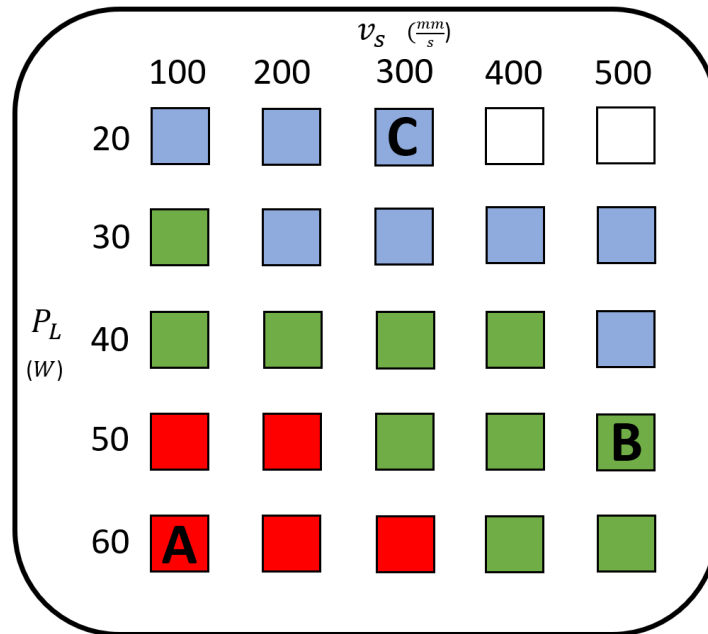


Figure 4.6: Overview: Groups of parameter sets based on surface analysis and choice of three representative samples A, B and C. Color code: Red is high, green is adequate and blue is low energy input

Table 4.3: Surface analysis of samples A, B and C, with comparison of SEM picture, EDX mapping and macroscopic picture of each sample's surface

	SEM	EDX	macroscopic
A			
B			
C			

4.3.1 High Energy Input

The parameter sets marked red in figure 4.3 form the group of the high energy input. The samples of this group are characterized by highly overlapping welding lines (table 4.1) and a surface swelling effect, which can be seen in the macroscopic picture in table 4.3 at sample A. This sample was produced with the combination of $P_L = 60 \text{ W}$ and $v_s = 100 \text{ mm/s}$, resulting in $E_v = 428.57 \text{ J/mm}^3$. This leads to circular surface elevations of up to 1 mm diameter which rise above the level of powder. This effect is also known from welding, where it is called humping welding. According to Manriquez-Frayre and Bourell [34] it can be related to the surface tension, but the topic is not completely understood at the moment and research is still being done [35]. These macroscopic humps have no influence on the microstructure, where an even appearance of welding lines can be seen in the SEM image. Furthermore, it was found that in this group of samples iron-rich and nickel-rich areas separate on the surfaces. Those areas are line-shaped and lie parallel to the welding lines. The EDX measurement of sample A is depicted in table 4.3, where the element occurrence is directly compared to the surface topology. In the SEM picture the welding lines can be seen clearly, and the EDX mapping shows areas with increased content of iron especially along the welding line edges. For further investigation, a second, more detailed EDX measurement was performed with longer measurement time and thus higher resolution. The result is shown in figure 4.7, where the focus is set on the local ratio of the elements. Therefore, the picture is divided into 3575 cells and the ratio of iron to nickel for each cell is mapped. In the iron-rich areas, ratios of $\frac{\text{at.\%Fe}}{\text{at.\%Ni}} = 2.5$ to 8 established. As a reference, the ratio of the mixed powder was approximately 0.27 in the mixture of $\text{Ni}_{78.5} - \text{Fe}_{21.5}$.

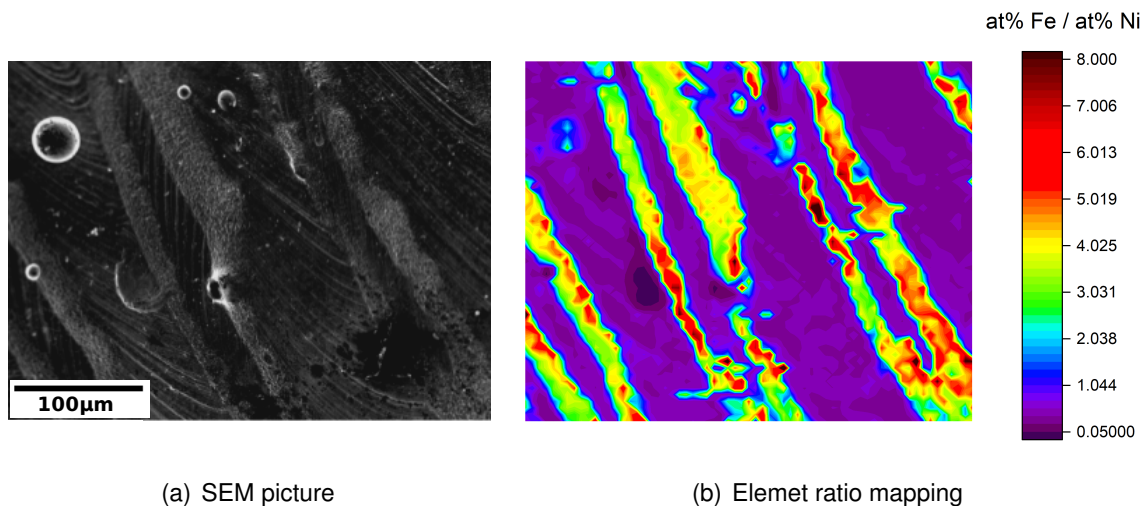


Figure 4.7: Comparison of SEM picture to mapped ratios of at.-% iron to at.-% nickel for each of the 3575 picture cells. Measured with SEM and EDX on the upper surface of sample A. A segregation of iron and nickel along the welding lines can be seen along with ratios between 0.05 and 8

The reason for the line-shaped segregations of iron and nickel on the surface is assumed to be related to the marangoni convection, which results in material flows within the melting pool.

According to J. Brillo and I. Egry [36], the surface tension for iron is higher than for nickel, and decreases with increasing temperature for both elements. Furthermore, the surface tension is related to the Marangoni flow directions, according to Saldi [37]. However, the measured data is not sufficient to prove this assumption.

4.3.2 Adequate Energy Input

In the cubes produced with an adequate energy input, meaning with the parameter sets depicted in green color in figure 4.3, the welding lines are well connected and form a dense structure. This group is represented by sample B. A light form of balling can be seen, which means that the welding lines are not evenly shaped but form ball-shaped areas with a higher amount of material separated by areas with less material. This results in uneven welding line structures. This is shown in the example of representative sample B in table 4.3 for the process parameters $P_L = 50 \text{ W}$, $v_s = 500 \text{ mm/s}$ and $E_v = 71.43 \text{ J/mm}^3$. According to Li et al. [38], this can be caused by a lower E_v and thereby reduced wetting ability. This results in the formation of balls of material within the welding lines which are separated by holes. In this group of samples, the effect can be seen, but it has a minor impact on the process stability. Instead, from macroscopic view the sample has the requested dimensions with no super-elevations, but a low surface quality. Furthermore, it can be seen that the elements are distributed predominantly unevenly, but more homogeneous than sample A. Few microscopic defects such as holes or elevations appear on the surface while the macroscopic appearance is rather even. The building process is stable without major disruptions.

4.3.3 Low Energy Input

The production with low energy input leads to the formation of porous surfaces due to low connected welding lines. Holes and balls appear, and the shape of the welding lines or the direction of scan is hardly recognizable. The elements are not mixed, instead they co-exist in the porous structure. The representative sample C was produced with $P_L = 20 \text{ W}$, $v_s = 300 \text{ mm/s}$ and $E_v = 47.62 \text{ J/mm}^3$ and shows a surface structure and element distribution that is similar to the mixed powder in figure 4.3. This leads to the assumption that the single powder grains were not completely molten. The low E_v was sufficient to melt only the particle surfaces and thus causing a porous structure.

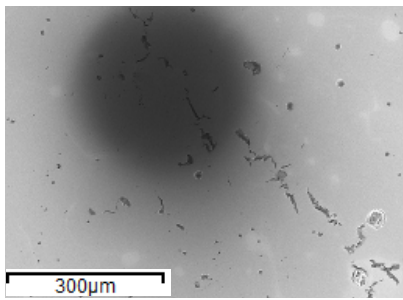
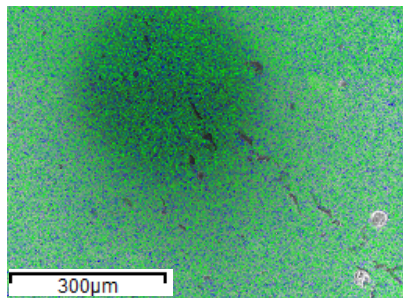
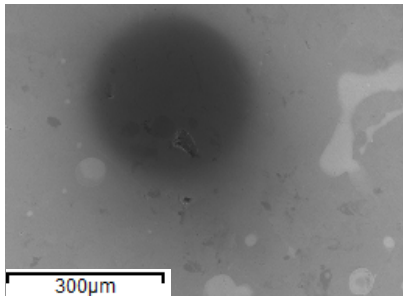
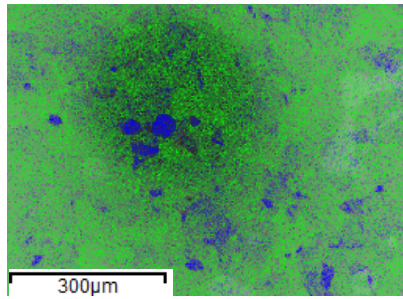
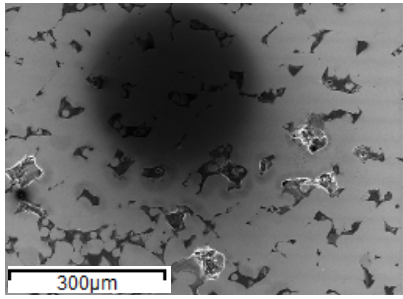
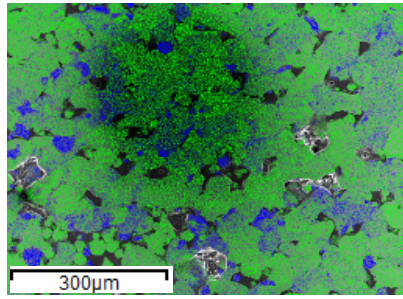
From this point on the samples A, B and C are used for further experiments as representatives for the high, adequate and low energy input.

4.4 Analysis of Bulk Material

EDX and SEM are surface-sensitive measurement methods. To discuss the microstructure and distribution of elements inside the samples, they are cut, embedded, grinded and polished (see p. 16). The described measurements are performed on the vertical (A-A) and horizontal cuts (B-B) to approximate the properties of the bulk material.

Firstly, an SEM and EDX measurement is performed on these cuts to examine the occurrence of iron and nickel. The results are depicted in table 4.4. For sample A, B and C, an SEM picture is shown next to the EDX mapping of the same area. The elements registered by EDX are colored, iron is blue and nickel is green. Thus the morphology can be directly compared to the element occurrence.

Table 4.4: Analysis of polished horizontal cuts A-A of samples A, B and C with SEM and EDX

Sample	SEM	EDX
A		
B		
C		

For sample A a mostly homogeneous distribution is found. In the SEM pictures, besides black pores, small circles of lighter colored material can be seen. This effect can not directly be related to a change in composition in these areas, as the occurrence of iron and nickel seems to be distributed homogeneously. In contrast to the upper surface of this sample, no agglomerations

or line-shaped segregations can be seen here.

Sample B shows a less homogeneous element distribution. The SEM picture indicates areas with a lighter color, black pores and other areas with a darker color than the main part of the bulk material. The related EDX mapping indicates that the dark shaded regions are rich of iron and thus can be related to a material contrast in the SEM. To evaluate the contrast in the SEM picture and the relation to material differences more detailed, an extended EDX mapping was performed and the results are shown in figure 4.8. The materials appearing in a darker color are related to a ratio of iron to nickel of more than 8, which refers to concentrations of more than 80% iron. On the contrary, around the pore in the lower left corner no remarkable changes in composition are found. Iron has an atomic number of 26 which is smaller than the number of 28 for nickel. Hence, nickel is heavier and the backscattered electrons can be reflected more effectively at the nickel atoms. Areas with high amount of iron instead show a lower capability to reflect backscattering electrons, the detector registers a lower intensity and thus the corresponding image area is depicted in a darker shade. Equally to sample A, the light colored areas of sample B are not related to changes in distribution. Additionally the surface was polished before the measurement. It can be concluded that neither topology nor material contrast are causing the occurrence of these light shaded areas. Possibly a local change of the crystal structure could be the reason for the change in contrast.

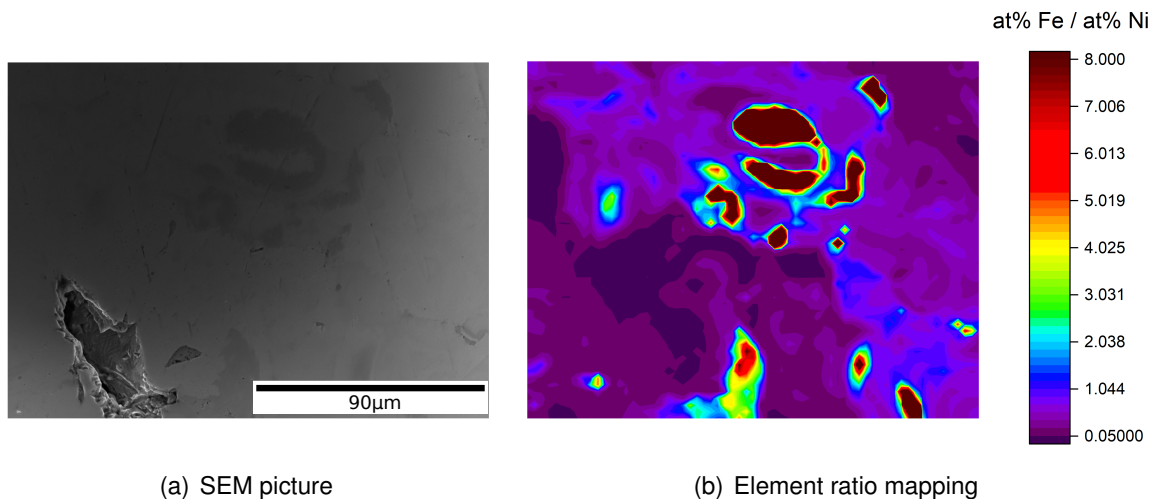


Figure 4.8: Comparison of SEM picture to mapped ratios of at.-% iron to at.-% nickel for each of the 3757 picture cells. Measured with EDX at horizontal cut A-A of sample B

For sample C the broad measurement of the cut surfaces shows clearly separated and irregularly distributed zones of either high iron or high nickel concentrations combined with a highly porous structure. Comparing this analyzed cut to the mixed powder (shown in figure 4.3 (b)) strong similarities can be seen in the distribution of iron and nickel and in the structure of the material. The spherical shape of the powder grains still can be seen. Thus it can be concluded that the volume energy density was not sufficient to melt and mix the particles and elements but rather

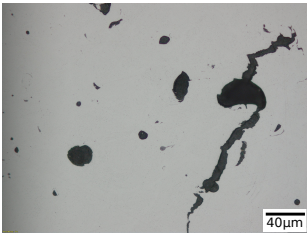
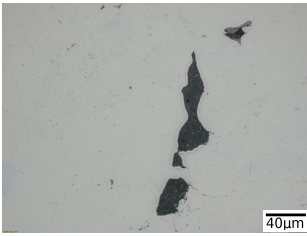
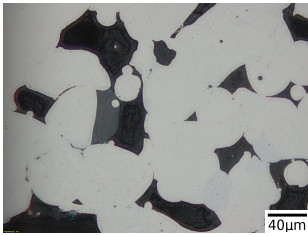
melt and connect their surfaces .

The vertical and horizontal cuts show no difference in element distribution or structure. The corresponding pictures of the vertical cut B-B can be found in the appendix. Based on these observations it can be concluded that the element distribution and structure are uniform throughout the bulk material.

4.5 Density and Pores

The density of samples A, B and C was measured by analyzing light microscopic images (see p. 17). The measurement is based on four pictures at 5x magnification of the horizontal cut A-A and on two pictures of the vertical cut B-B. The results and pictures of specific pores at higher magnification are presented in table 4.5. Sample C has the lowest density, which can be reasonably connected to the low energy input. Sample A and B are almost equal with a very high density, although sample B is with $\approx 98.5\%$ the most dense sample. The picture of sample A shows cracks and spherical pores, whereas in sample B a randomly shaped pore can be seen.

Table 4.5: Light microscopic images of polished surfaces at horizontal cut A-A of the representative cubes A, B and C. Characteristic pore shapes are shown together with the mean density

Cut	A	B	C
Picture			
Density A-A	97.75%	98.22%	80.45%
Density B-B	97.56%	98.97%	82.73%

The different shape of the pores of sample A, B and C leads to the assumption that differently shaped pores have different origins. These are assumed to relate to the volume energy density. In sample C the low energy input was insufficient to completely melt the material, which caused pores with irregular shape and size. During the building process the powder particles were molten only on their surfaces, thus the spherical shape of single grains is still visible. By comparing samples C and B it can be seen that the pore size decreases. Thus it can be said that with rising energy input the density increases. The unevenly shaped pore of sample B indicates an area between some particles that are not connected completely, but no specific particle can be seen. Sample A has the highest E_v . In the related picture, cracks and spherical pores can be seen. The cracks could be caused by high stresses induced by high local temperature gradients during the building process. The spherical pores could be results

of evaporated material, bubbles of process gas or oxygen from the decomposition of oxidized powder particles.

4.6 Crystal Phase Analysis

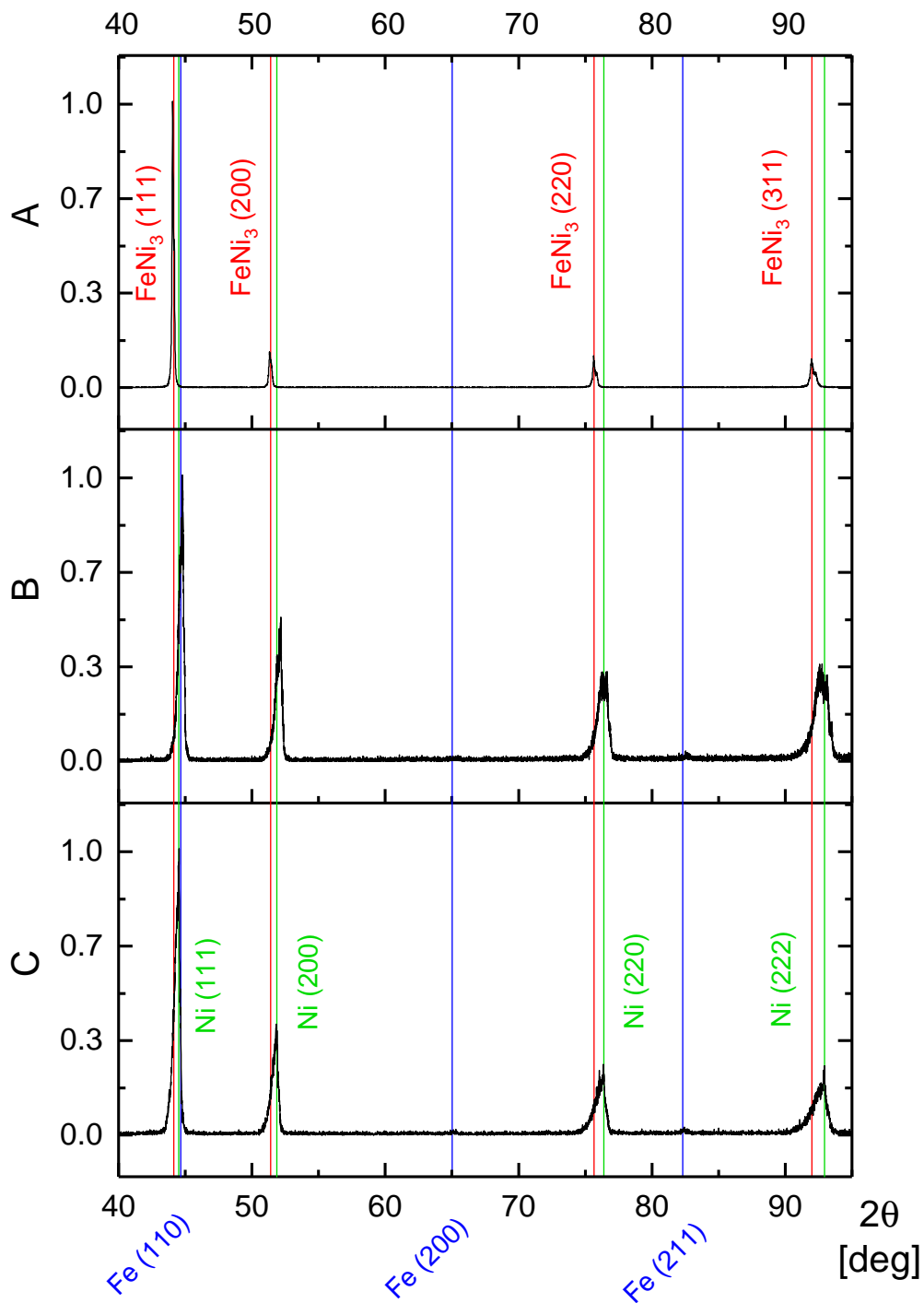


Figure 4.9: Diffractogramm of polished surfaces of samples A, B and C. The intensity is normalized for each sample. Peaks of sample A coincide with FeNi_3 , those of sample B and C coincide with Ni phase

The crystal phase of the samples was analyzed with an X-Ray diffraction measurement on the polished surfaces of the horizontal cuts (A-A). The results are depicted in the diffractograms in figure 4.9. For all three samples the first and highest peak is registered at an angle between 44° and 45° . It can be seen that this peak of sample A is slightly shifted to a smaller angle in comparison to B and C. Additionally, the positions as well as the relative intensities for the peaks at higher orders are different for sample A on one hand and samples B and C on the other hand. For sample A the peaks coincide best with the reference peaks of fcc $FeNi_3$, while the peaks of samples B and C relate to those of pure fcc Ni .

Furthermore, the intensities of the (200), (220) and (311) peaks have a 90% lower intensity than the (111) peak at sample A. According to the reference values, in a polycrystalline $FeNi_3$ phase without texture the (200) peak should have about 43% intensity, the (220) peak 19% and the (311) peak 18% of the (111) peak, respectively. Hence, the measured values are lower than expected. This indicates a strong (111) texture perpendicular to the surface for sample A. Due to the small width of the XRD peaks and low intensity of the background noise a good crystal quality can be assumed. For B and C, the (200) peak has an intensity of more than 30%, while the (220) and (222) peaks show a reduced intensity of 15 to 30%. This correlates with the expected values for pure fcc Ni , thus a polycrystalline phase can be assumed here. This is supported by the broader width of the peaks and visible background noise in the diffractogram. None of the diffractograms has peaks related to the reference lines of pure iron.

The high amount of nickel in the $Ni_{78.5} - Fe_{21.5}$ mixture leads to the suppression of the peaks related to iron. Additional measurements were performed on samples of the mixed powder and each single powder. In the resulting diffractogram only nickel-related peaks were registered for the powder mixture. The single powders showed characteristic peaks for iron and nickel, respectively. It was striking that the total intensity registered in the (111) peak of the nickel powder was nine times higher than the one of the iron powder. This explains the suppression of the iron-related peaks in the measurement of the mixed powder. Thus, the nickel-related peaks registered in mixed powder as well as in samples B and C correspond to the particle mixture and not to the phase of the alloyed material. It can be assumed that only in sample A the volume energy density was sufficient to form the $FeNi_3$ phase. In sample B and C the energy input and the time the material was exposed to the laser was not sufficient to create a melting pool with a homogeneous mixture of elements. In the solidified state, the coexisting elements can be seen (table 4.4), which supports the assumption that despite the correct total composition, local inhomogeneities occur as a result of the low E_v . Thus, it can be said that the iron and nickel phases coexist and the $FeNi_3$ phase could not form.

4.7 Analysis of Magnetic Properties

The magnetic properties of the 3 mm cubes are determined with a VSM. The resulting magnetization curves can be seen in figure 4.10, 4.11 and 4.12 for sample A, B and C, respectively. The magnetization curves $M(H)$ were recorded at an applied field parallel and perpendicular to the z-axis of the LBM process. Additionally, the powder was measured and a comparison to the results of the parallel measurements of all three samples is presented in figure 4.13.

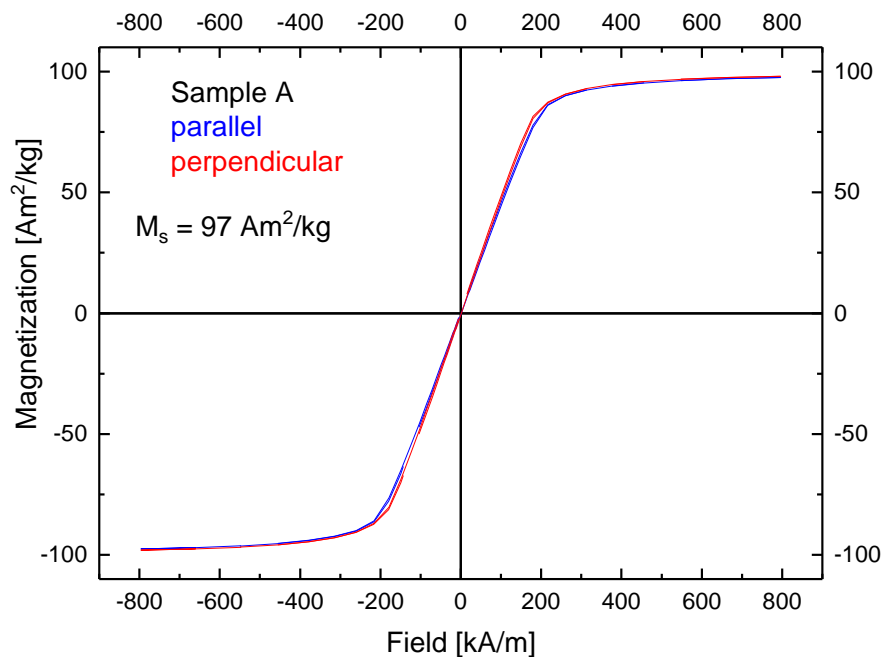


Figure 4.10: Magnetization curve of the sample A, measured by VSM

The typical shape for ferromagnetic magnetization curves can be observed for all samples: At a low external field, the slope of the $M(H)$ curve is high, until the magnetization approaches the saturation point. The hysteresis is very small and the remanence and coercivity of almost zero indicate a very soft magnetic response of the samples.

The differences between the perpendicular and parallel measurements are not of a noticeable significance for sample A and B. Sample C shows a slightly faster increase in magnetization with increasing field for the magnetic field applied perpendicular to the z-axis of the building process (see figure 4.12). In this orientation, the magnetization reaches its saturation level at a slightly lower field intensity. The difference in the development of the magnetization curves $M(H)$ corresponding to perpendicular and parallel external field is related to a small magnetic anisotropy of the sample. This anisotropy can originate from the shape and / or the magnetocrystalline anisotropy which may include magnetoelastic anisotropy (magnetostriction). However, the difference in $M(H)$ for the different orientations is very small and it can be

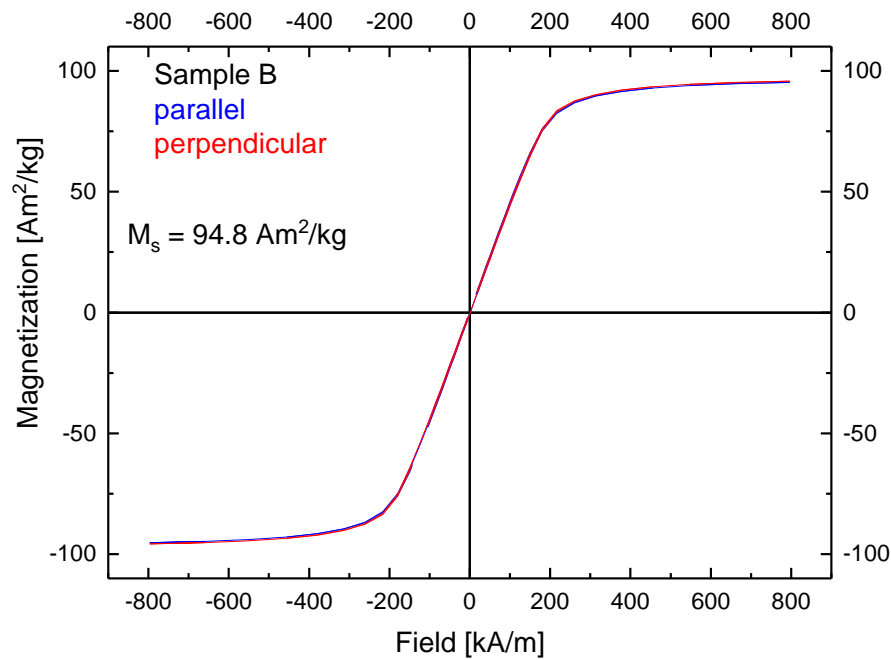


Figure 4.11: Magnetization curve of the sample B, measured by VSM

concluded that no sufficient magnetic anisotropy induced by the LBM building process is found.

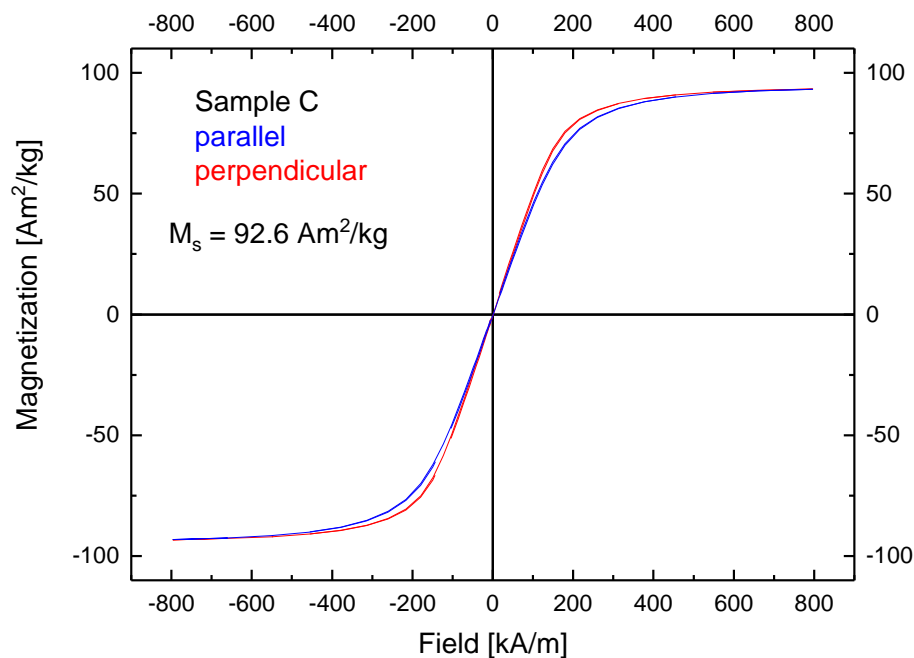


Figure 4.12: Magnetization curve of the sample C, measured by VSM

In figure 4.13 a direct comparison of the magnetization curves for samples A, B, C and the powder blend is given. The differences can be seen in the saturation magnetization as well

as in the development of $M(H)$. For the powder, a linear increase of M is measured at a low external field of up to 100 kA/m . For the samples produced by LBM, the linear increase of M is expanded to an external field of up to 180 kA/m .

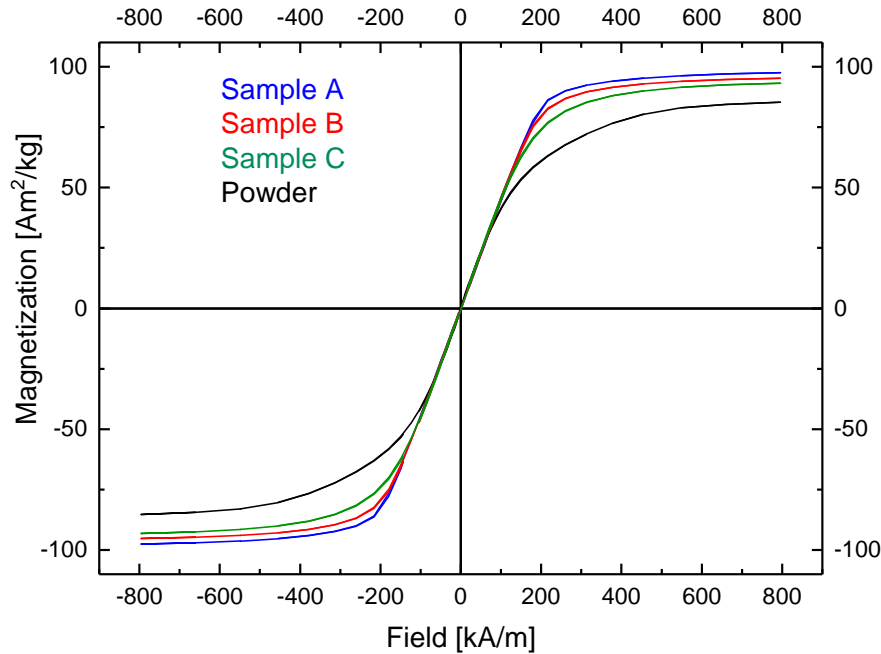


Figure 4.13: Comparison of magnetization curves of the samples A, B, C and powder blend. The external field is applied parallel to the z-axis of the LBM process for cubic samples

The saturation magnetization and the volume energy density of the samples and powder are presented in table 4.6. The blended powder material has the lowest saturation magnetization of $85 \text{ Am}^2/\text{kg}$. For the LBM samples it was found that with an increasing volume energy density the saturation magnetization increases to $92.6 \text{ Am}^2/\text{kg}$ for sample C and to $97 \text{ Am}^2/\text{kg}$ for sample A. Comparing samples A and C, the increase in E_v of 900% leads to an increase in M_s of about 5%. M_s of sample A is about 14% higher than of the powder blend. The difference between samples B and C is already 2% in M_s and 153% in E_v . The difference in M_s caused by the change of process parameters reaches up to 4.7% comparing sample C to A.

Table 4.6: Comparison of saturation magnetization M_s of samples A, B, C and powder to their volume energy density E_v applied during the LBM process

Sample	$M_s \left(\frac{\text{Am}^2}{\text{kg}} \right)$	$E_v \left(\frac{\text{J}}{\text{mm}^3} \right)$
A	97	428.57
B	94.8	73.41
C	92.6	47.62
Powder	85	-

A possible explanation for the increase in M_s could be based on the different phases registered in

the XRD measurements. Only in sample A the phase of $FeNi_3$ is registered. Thus the theoretical difference in magnetization of the powder blend to the $FeNi_3$ phase can be calculated and compared to the measured increase. Therefore the powder blend is assumed to be a mixture of pure iron and pure nickel, which can be described by Vegard's Rule. The characteristics of the single elements are given: Iron has a magnetic moment of $2.2\mu_B$ per atom and the number of $e_{Fe} = 26$ electrons per atom, while nickel has $0.6\mu_B$ per atom and $e_{Ni} = 28$ electrons (see figure 4.14). According to Vegard's Rule, the properties of a mixture of elements can be derived by linear interpolation of the single element's properties. Thus the magnetic moment at the saturation magnetization of $Ni_{78.5} - Fe_{21.5}$ powder is calculated as $m_{powder,th} = 0.91\mu_B$ per atom. For the alloyed material, the Slater-Pauling curve in figure 4.14 has to be considered. For the alloy of $Ni_{78.5} - Fe_{21.5}$ holds:

$$e_{FeNi_3} = at. - \%Ni \cdot e_{Ni} + at. - \%Fe \cdot e_{Fe} = 0.785 \cdot 28 + 0.215 \cdot 26 = 27.57 \quad (4.1)$$

Therefore, the alloy is assumed to possess 27.57 electrons per atom on average. In the Slater-Pauling curve, this is related to a magnetic moment of $m_{FeNi_3,th} = 1\mu_B$ per atom. [18]

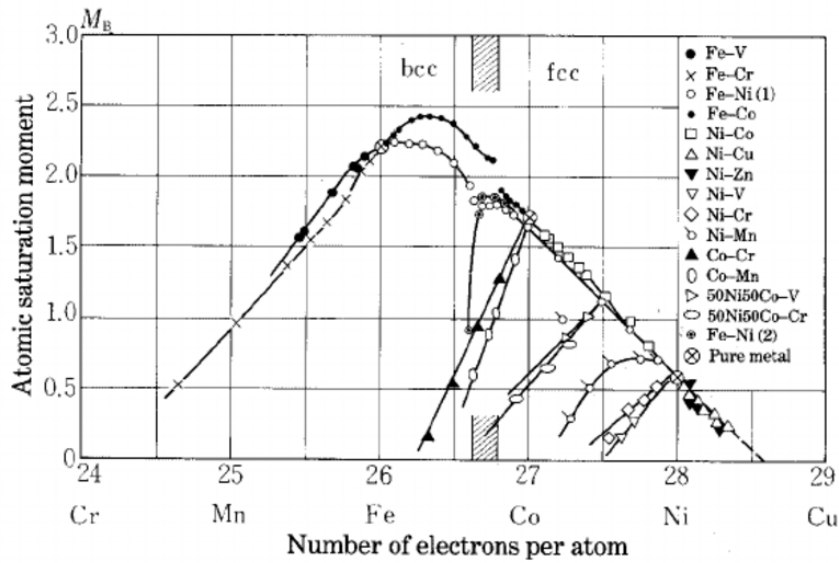


Figure 4.14: The Slater-Pauling curve relates the average atomic moment at saturation to the number of elements in an alloyed material [39]

The difference in saturation magnetization from a mixed powder to the alloy in theory and experiment is:

$$\Delta_{th} = (m_{FeNi_3,th} / m_{powder,th}) - 1 = (1 / 0.91) - 1 = 0.099 \quad (4.2)$$

$$\Delta_{exp} = (M_{sample A} / M_{powder}) - 1 = (97 / 85) - 1 = 0.141 \quad (4.3)$$

For the experimental values, the mass magnetization saturation measured at 300 K were used.

Due to the obtained data the measured difference in magnetization can be explained only partly by considering the Slater-Pauling curve. Possibly an oxidation of the powders causes the higher measured difference.

However, it can be stated that the volume energy density is related to the resulting saturation magnetization, although the physical reason could not be explained completely.

5 Conclusions

The aim of this work was the correlation between the process parameters in LBM, the distribution of elements in the produced samples and the resulting structural and magnetic properties based on a binary powder blend. As raw materials two mostly pure powders were used, one of iron and one of nickel. The powder grains are mostly spherical and have a diameter of up to $55\text{ }\mu\text{m}$, the maximum of the relative volume distribution is between 30 and $40\text{ }\mu\text{m}$ for both powders. A good mixture of the composition $Ni_{78.5} - Fe_{21.5}$ was found after mixing the blend with the Turbula principle in a glass container for 25-30 min. 23 from 25 samples with different combinations of laser power and scanning velocity were successfully produced. They were classified to three groups of samples by similar structures and element distributions on the surfaces. Representatives of these groups were used for the investigation of the structure, element distribution, density and crystal phase on cut surfaces. The magnetic properties were measured using cubic samples of the representative parameter sets for each group.

The group with the highest volume energy density is represented by sample A. It was produced with an energy input of $E_v = 428.57\text{ J/mm}^3$. Samples of this group show a macroscopic surface swelling with a size of up to 1 mm, which leads to an instable production process. A high overlap of welding lines could be seen, the even microstructural appearance is not influenced by the surface swelling. A line-shaped segregation of iron and nickel along the welding lines is found on the upper surface while in the vertical and horizontal cuts the elements are distributed homogeneously. Spherical pores and cracks are visible, a density of 97.6% is reached. The XRD analysis indicates the $FeNi_3$ phase with a strong (111) texture. The saturation magnetization $97\text{ Am}^2/\text{kg}$. Thus in this sample the binary powder mixture was successfully and homogeneously alloyed.

The second group of samples is produced with an adequate energy input which leads to a reliable building process. The representative sample B has an energy input of $E_v = 73.41\text{ J/mm}^3$. A good connection of the welding lines and the single layers as well as the highest measured density of 98.5% is achieved. Small pores and a partly homogeneous distribution of elements are found, as well as a saturation magnetization of $M_s = 94.8\text{ Am}^2/\text{kg}$.

The last group consists of samples produced with a low energy input. Sample C with the lowest possible volume energy density of $E_v = 47.62\text{ J/mm}^3$ represents this group. It is characterized by a porous surface structure on the top and in the cuts and leads to the low density of 81.6%. The elements are not uniformly distributed. Thus, it can be said that the powder grains were molten only on their surfaces, leading to a connection of single powder grains, which is also known as sintering. The saturation magnetization reaches a value of $92.6\text{ Am}^2/\text{kg}$.

The comparison of the three samples A, B and C shows that a low energy input melts the powder particles only on their surfaces. With an increasing energy input, the porosity decreases. The highest input is sufficient to form a liquid melting pool for a time long enough to enable a homogeneous mixture of iron and nickel. The result is a $FeNi_3$ phase and an increase in M_s of 14% compared to the mixed powder.

This work successfully related the increase in volume energy density to an increasing element homogeneity and to an increasing saturation magnetization for the processed samples based on the binary powder blend $Ni_{78.5} - Fe_{21.5}$. The measured magnetic properties are matching the expected values for permalloy bulk material and those achieved by Zhang et al. [6]. The inhomogeneities detected by Bauer et al. [7] could be related to a change of the saturation magnetization. Thus it was found that by the choice of process parameters not only the structural, but also the magnetic properties of the resulting material can be altered.

A high increase of the saturation magnetization was found in the single-phase $FeNi_3$ sample produced with the highest volume energy density. This measured increase was higher than calculated by application of Vegard's Rule and Slater-Pauling curve. It can be assumed that the amount of oxygen in the powder has an influence on the magnetization of the powder. To check this assumption, the influence of storage conditions of the powder on its magnetic properties could be investigated.

EDX measurements further revealed a segregation of iron and nickel on the upper surface of samples produced with high volume energy density. This effect was not found within the bulk material. A relation to temperature-induced changes in surface tension and the marangoni convection can be assumed. Additional experiments could help to understand the formation of the segregation. For example, the resulting temperatures in the melting pool could be measured or simulated in order to estimate the influence of the heat-dependent surface tensions of iron and nickel on the formed structure. Furthermore, monolayer experiment could be performed with scanning the same layer of powder once, twice or thrice to investigate the influence of an increased energy input per layer on the element distribution.

List of References

- [1] SEHRT, J. T.: *Möglichkeiten und Grenzen bei der generativen Herstellung metallischer Teile durch das Strahlschmelzverfahren*. Shaker, 2010. – PhD Thesis
- [2] KLESZCZYNSKI, S.: *Qualifizierung von Eisen-Nickel Legierungen für den Strahlschmelzprozess unter Berücksichtigung der mechanischen und thermischen Materialeigenschaften*, Universität Duisburg-Essen, Diplomarbeit, 2016
- [3] GEBHARDT, A. ; HÖTTER, J.-S.: *Additive manufacturing: 3D printing for prototyping and manufacturing*. Munich / Cincinnati : Hanser Publishers, 2016
- [4] N., N.: *DIN EN ISO / ASTM 52900: Additive Fertigung - Grundlagen - Terminologie*, Juni 2017
- [5] JAĆIMOVIĆ, J. ; BINDA, F. ; HERRMANN, L. G. ; GREUTER, F. ; GENTA, J. ; CALVO, M. ; TOMŠE, T. ; SIMON, R. A.: Net Shape 3D Printed NdFeB Permanent Magnet. In: *Advanced Engineering Materials* (2017)
- [6] ZHANG, B. ; FENINECHE, N.-E. ; LIAO, H. ; CODDET, C.: Magnetic properties of in-situ synthesized FeNi 3 by selective laser melting Fe-80% Ni powders. In: *Journal of Magnetism and Magnetic Materials* 336 (2013), p. 49–54
- [7] BAUER, T. ; SPIERINGS, S. ; WEGENER, K.: Investigations of mixing behaviour of binary nickel-iron blends using SLM. In: *Rapid.Tech - International Trade Show and Conference for Additive Manufacturing* (2017), p. 377–390
- [8] WITT, G. ; SAUER, A. ; WITT, G. (Ed.): *Taschenbuch der Fertigungstechnik : mit zahlreichen Tabellen*. München [i.a.] : Fachbuchverl. Leipzig im Carl-Hanser-Verl., 2006
- [9] BERGER, U.: *Additive Fertigungsverfahren : rapid prototyping, rapid tooling, rapid manufacturing*. 1. Haan-Gruiten : Verlag Europa-Lehrmittel Nourney, Vollmer, 2013
- [10] FISCHER, U.: *Tabellenbuch Metall*. Europa-Lehrmittel, 2011 (Europa-Fachbuchreihe für Metallberufe)
- [11] ZÄH, M. (Ed.): *Wirtschaftliche Fertigung mit Rapid-Technologien : Anwender-Leitfaden zur Auswahl geeigneter Verfahren*. München [i.a.] : Hanser, 2006
- [12] N., N.: *VDI 3405: Additive manufacturing processes, rapid manufacturing - Basics, definitions, processes*, Dezember 2014

- [13] *Wohlers Report : Additive manufacturing and 3D printing state of the industry ; Annual worldwide progress report. 2016.* Fort Collins, Colo. : Wohlers Associates, 2016
- [14] EOS GMBH: *webpage.* url: <https://www.eos.info/>, Oktober 2017
- [15] MEINERS, W.: *Direktes selektives Laser-Sintern einkomponentiger metallischer Werkstoffe; Als Ms. gedr.* Aachen : Shaker, 1999 (Berichte aus der Lasertechnik). – PhD Thesis
- [16] STEVENSON, A. (Ed.): *Concise Oxford English dictionary.* 12. Oxford [i.a.] : Oxford Univ. Press, 2011
- [17] CHUNG, D. D. L.: *Functional materials : Electrical, dielectric, electromagnetic, optical and magnetic applications ; (with companion solution manual).* New Jersey [i.a.] : World Scientific, 2010
- [18] KRISHNAN, K.M.: *Fundamentals and Applications of Magnetic Materials.* OUP Oxford, 2016
- [19] GROSS, R. ; MARX, A.: *Festkörperphysik. 2.* Berlin / Boston : De Gruyter Oldenbourg, 2014
- [20] HEINTZE, J. ; BOCK (ED.), P.: *Lehrbuch zur Experimentalphysik Band 3: Elektrizität und Magnetismus. 1.* Berlin / Heidelberg : Springer Berlin Heidelberg, 2016
- [21] ARNOLD, H.D. ; ELMEN, G.W.: Permalloy, an alloy of remarkable magnetic properties. In: *Journal of the Franklin Institute* 195 (1923), no. 5, p. 621–632
- [22] ELMEN, G.W.: Magnetic alloys of iron, nickel, and cobalt. In: *Journal of the Franklin Institute* 207 (1929), no. 5, p. 583 – 617
- [23] VERNYHORA, I. ; TATARENKO, V. ; M. BOKOCH, S: Thermodynamics of f.c.c.-Ni–Fe Alloys in a Static Applied Magnetic Field. In: *ISRN Thermodynamics* 2012 (2012)
- [24] BARGEL, H.-J. (Ed.): *Werkstoffkunde. 11.* Berlin / Heidelberg : Springer Berlin Heidelberg, 2012
- [25] LU, X. ; LIANG, G. ; ZHANG, Y.: Synthesis and characterization of magnetic FeNi₃ particles obtained by hydrazine reduction in aqueous solution. In: *Materials Science and Engineering: B* 139 (2007), no. 2, p. 124 – 127
- [26] WILLY A. BACHOFEN AG - MASCHINENFABRIK: *Data Sheet Turbular.* url: <http://www.wab.ch/en/mixer/turbular.html>, Oktober 2017

- [27] N., N.: *DIN EN ISO 3923.1:2010 Metallpulver - Ermittlung der Füllichte - Teil 1: Trichterverfahren*, August 2010
- [28] N., N.: *DIN EN ISO 4490:2014 Metallpulver - Ermittlung der Durchflussrate mit Hilfe eines kalibrierten Trichters (Hall flowmeter)*, November 2014
- [29] SHISHKOVSKY, I. ; SAPHRONOV, V.: Peculiarities of selective laser melting process for permalloy powder. In: *Materials Letters* 171 (2016), p. 208–211
- [30] REICHELT, R.: Scanning Electron Microscopy. In: HAWKES, P. W. (Ed.) ; SPENCE, J. C. H. (Ed.): *Science of Microscopy*. New York : Springer New York, 2007, p. 133–272
- [31] DEMERS, H. ; POIRIER-DEMERS, N. ; COUTURE, A. R. ; JOLY, D. ; GUILMAIN, M. ; JONGE, N. de ; DROUIN, D.: Three-dimensional electron microscopy simulation with the CASINO Monte Carlo software. In: *Scanning* 33 (2011), no. 3, p. 135–146
- [32] SPIESS, L. ; SCHWARZER, R. ; BEHNKEN, H. ; TEICHERT, G.: *Moderne Röntgenbeugung: Röntgendiffraktometrie für Materialwissenschaftler, Physiker und Chemiker*. Vieweg+Teubner Verlag, 2005
- [33] FONER, S.: Vibrating Sample Magnetometer. In: *Review of Scientific Instruments* 27 (1956), no. 7, p. 548–548
- [34] MANRIQUEZ-FRAYRE, J.A. ; BOURELL, D.L.: Selective laser sintering of binary metallic powder. In: *Proceedings of the Solid Freeform Fabrication Symposium, The University of Texas at Austin, Austin, TX Bd. 94*, 1990
- [35] SEILER, M. ; PATSCHGER, A. ; TIANIS, L. ; ROCHHOLZ, C. ; BLIEDTNER, J.: Experimental determination of influencing factors on the humping phenomenon during laser micro welding of thin metal sheets. In: *Journal of Laser Applications* 29 (2017), no. 2, p. 022413
- [36] BRILLO, J. ; EGRY, I.: Surface tension of nickel, copper, iron and their binary alloys. In: *Journal of Materials Science* 40 (2005), no. 9, p. 2213–2216
- [37] SALDI, Z. S.: *Marangoni driven free surface flows in liquid weld pools*. Delft, Delft University of Technology, PhD Thesis, 2012
- [38] LI, R. ; LIU, J. ; SHI, Y. ; WANG, L. ; JIANG, W.: Balling behavior of stainless steel and nickel powder during selective laser melting process. In: *The International Journal of Advanced Manufacturing Technology* 59 (2012), no. 9, p. 1025–1035
- [39] BOZORTH, R. M.: *Ferromagnetism*. 1993. – 992 S.

List of Figures

2.1	Sketch of the process steps for laser beam melting	4
2.2	Process parameters in Laser Beam Melting for a bi-directional alternating stripe scanning strategy. In a single layer, the laser scans the surface stripe-wise in positive and negative scan axis. This axis is alternating between x and y axis for each new layer [1]	5
2.3	Hysteresis of a ferromagnetic material showing the magnetization M in dependence on the external field H with saturation magnetization M_s , remanence M_r and coercive field H_c [20]	8
2.4	The binary phase diagram of the Fe-Ni system with superstructures (\circ = Ni, \bullet = Fe) [23]. At 78.5 at.-% Ni a $FeNi_3$ phase and the $L1_2$ superstructure can be expected	11
2.5	Effect of heat treatment and composition on initial permeability of nickel-iron-alloys for air quenched (cooling rate of $20^\circ C/sec$), annealed ($1.5^\circ C/min$) and baked (held at $425^\circ C$ for 24h) alloys [22]	12
3.1	CAD design of the samples, dimensions are given in mm	15
3.2	Sketch of the directions of cut: Horizontal A-A and vertical B-B	17
3.3	Bragg-Brentano geometry for XRD. The X-ray tube and the detector move around the sample with the angle θ	18
3.4	Sketch of a Vibrating Sample Magnetometer including a reference sample. (1) transducer, (2) inlet support, (3) sample holder, (4) reference sample, (5) sample, (6) reference coils, (7) sample coils, (8) field-inducing magnet poles, (9) metal container [33]	18
3.5	Orientation of sample cube in VSM: The parallel external field is oriented along the building direction z, the perpendicular field orthogonal to it	19
4.1	Size distributions of the single input powders, based on analysis of 10 SEM pictures for each element	20
4.2	Size and shape of input powders particles. Colors: Fe = blue, Ni = green, C = red	21
4.3	Particle distribution in the mixed powder after 30 min mixing	21
4.4	Variation of the measured mixing ratio r depending on the mixing time. After 25 min the mixture approaches the desired ratio of 0.274 according to equation (3.1)	22

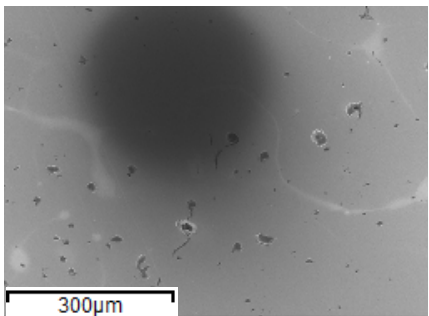
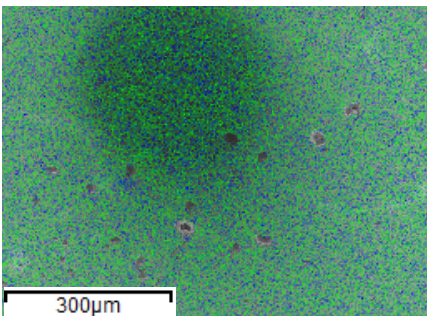
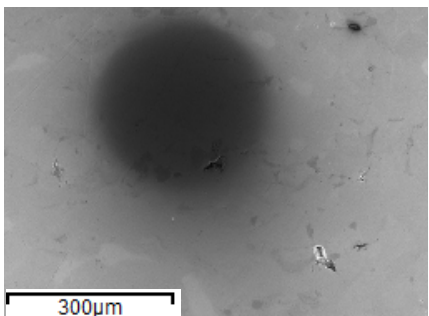
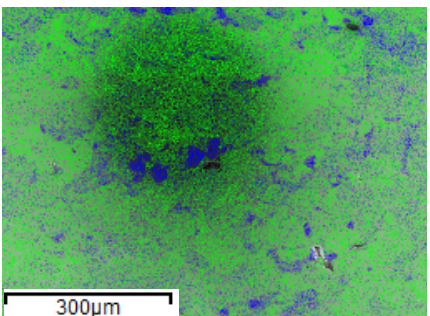
4.5	Photo of the platform with built samples before separating the samples from the platform. Parameters: $P_L = 20\text{ W}$ to 60 W and $v_s = 100\text{ mm/s}$ to 500 mm/s . Different surface structures are visible, especially at high energy input a surface swelling can be seen	23
4.6	Overview: Groups of parameter sets based on surface analysis and choice of three representative samples A, B and C. Color code: Red is high, green is adequate and blue is low energy input	26
4.7	Comparison of SEM picture to mapped ratios of at.-% iron to at.-% nickel for each of the 3757 picture cells. Measured with SEM and EDX on the upper surface of sample A. A segregation of iron and nickel along the welding lines can be seen along with ratios between 0.05 and 8	27
4.8	Comparison of SEM picture to mapped ratios of at.-% iron to at.-% nickel for each of the 3757 picture cells. Measured with EDX at horizontal cut A-A of sample B	30
4.9	Diffractiongram of polished surfaces of samples A, B and C. The intensity is normalized for each sample. Peaks of sample A coincide with $FeNi_3$, those of sample B and C coincide with Ni phase	32
4.10	Magnetization curve of the sample A, measured by VSM	34
4.11	Magnetization curve of the sample B, measured by VSM	35
4.12	Magnetization curve of the sample C, measured by VSM	35
4.13	Comparison of magnetization curves of the samples A, B, C and powder blend. The external field is applied parallel to the z-axis of the LBM process for cubic samples	36
4.14	The Slater-Pauling curve relates the average atomic moment at saturation to the number of elements in an alloyed material [39]	37

List of Tables

3.1	Selected process parameters for the LBM building process	14
4.1	SEM-pictures in dependence on the used laser power and scanning velocity during the building process	24
4.2	EDX mappings of samples produced with different laser powers and scanning velocities showing the occurrence of nickel (green) and iron (blue)	25
4.3	Surface analysis of samples A, B and C, with comparison of SEM picture, EDX mapping and macroscopic picture of each sample's surface	26
4.4	Analysis of polished horizontal cuts A-A of samples A, B and C with SEM and EDX	29
4.5	Light microscopic images of polished surfaces at horizontal cut A-A of the repre- sentative cubes A, B and C. Characteristic pore shapes are shown together with the mean density	31
4.6	Comparison of saturation magnetization M_s of samples A, B, C and powder to their volume energy density E_v applied during the LBM process	36
.1	Direct comparison of SEM (left) and EDX mapping (right) of the inside at hori- zontal cut A-A (top) and vertical cut B-B (bottom) of sample A.	47

Appendix

Table .1: Direct comparison of SEM (left) and EDX mapping (right) of the inside at horizontal cut A-A (top) and vertical cut B-B (bottom) of sample A.

Sample	SEM	EDX
A		
B		
C	